Optimization of Flow Characteristics of Gas–Solid Separators Based on NSGA-II and Entropy-Weighted TOPSIS

Xuehong Wu [a,b*], Yiming Xiao [a], Jin Zhang [c], Dehua Yu [a], Yong Liu [a], Shang Mao [a], Yanping Du [d,*]

a School of Energy and Power Engineering, Zhengzhou University of Light Industry, Zhengzhou, Henan 450000, China;

b International Joint Laboratory for Efficient Energy Conversion and Utilization of Henan Province, Zhengzhou, Henan 450000, China;

c AnYang Cigarette factory, China Tobacco Henan Industrial Co., Ltd., AnYang 473001, China

d School of Engineering, Lancaster University, Lancaster LA14YW, UK

** Corresponding author: wuxh1212@163.com, y.du17@lancaster.ac.uk*

Abstract: To address the challenges of controlling particle loss rate and outlet purity in high-concentration particulate systems, this study develops a CFD-DDPM-based gas–solid two-phase flow model. Combined with the NSGA-II algorithm and the entropy-weighted TOPSIS method, the effects of feed velocity, suction pressure, and throwing device speed on separation performance are systematically analyzed. The results indicate that the SST k–ω turbulence model coupled with the dense discrete phase model can accurately simulate the internal flow field of the separator, with simulation errors controlled within 5%. Regression models for particle loss rate and outlet purity were established using the Box–Behnken design, yielding coefficients of determination (R^2) of 0.9724 and 0.9397, respectively. Significance analysis shows that feed velocity is the most influential factor. Based on these regression models, multi-objective optimization using the NSGA-II algorithm produced a set of Pareto-optimal solutions. The Pareto front was comprehensively evaluated using the entropy-weighted TOPSIS method, and the optimal parameter combination was determined as follows: feed velocity of 1.89 m/s, suction pressure of 6539 Pa, and throwing device speed of 350 rpm. Under these

conditions, the particle loss rate is 0.0387%, and the outlet purity reaches 98.9189%, with deviations between simulated and predicted values less than 2%. These findings provide theoretical support and engineering guidance for separation optimization of high-concentration particulate systems.
Keywords：Gas–solid two-phase flow; High-concentration particulate system; CFD-DDPM simulation; NSGA-II; Entropy Weight TOPSIS;

1. Introduction

In numerous particle processing and separation systems, the efficient classification of particles with distinct physical properties continues to be a central focus in gas–solid two-phase flow engineering. The core of particle separation lies in achieving the precise separation of materials based on physical attributes such as particle size, density, and shape, typically achieved through airflow or gravitational fields. This technique has been widely applied in critical industrial processes such as stem–shred separation [1], seed screening and grain impurity removal in agriculture [2], dry classification in mineral processing [3], and raw material refinement in the food industry [4]. Common dry separation equipment used in these applications includes air classifiers, cyclone separators [5], and jet classifiers [6], all of which rely on differences in particle motion within high-velocity airflow to improve separation efficiency and ensure product purity.

However, despite widespread application, air classification systems often face challenges related to the instability of particle separation. Studies have shown that coupled phenomena, such as flow field non-uniformity, particle agglomeration, and cross-flow, are the primary contributors to fluctuations in separation efficiency. For instance, Zhang et al. [7] reported that adverse flow structures, including axial back-flow, short-circuiting, and eccentric recirculation within cyclone separators, significantly degrade separation performance. Additionally, particle agglomeration and attrition within the separator also play significant roles. Mirzaei et al. [8] demonstrated that under high particle concentration conditions, neglecting fine particle agglomeration in simulations

can lead to a considerable underestimation of separation efficiency, by as much as 5%–15%. Haig et al. [9] observed fine particle agglomeration during experiments with a Stairmand cyclone separator and found that the separation efficiency curves shifted notably with changes in inlet velocity. Against this backdrop, researchers have explored improvements to internal flow structures to enhance separation stability. For example, Petit et al. [10] proposed a throat classifier that effectively reduced fine-particle cross-flow and improved particle size distribution by modifying the airflow pathway. These findings suggest that even without altering the equipment structure, comparable separation performance can be achieved through appropriate adjustment of process parameters. Thus, systematically analyzing the effects of operational parameters on particle dynamics and optimizing performance accordingly has become a central focus in contemporary air classification research.

To further explore the coupling mechanisms between process parameters and particle behavior, previous studies have systematically investigated the interactions among key variables, including airflow velocity distribution, particle mass flux, and particle trajectories. Zhao et al. [11] conducted CFD–DEM simulations of pneumatic conveying and found that the combined effects of airflow velocity and particle concentration govern the stability of particle trajectories. When the flow velocity falls below a critical threshold, particle deposition increases significantly, leading to a roughly 40% reduction in conveying uniformity. Chakravarty et al. [12,13] investigated vortex vibratory screens and showed that when the airflow inclination exceeds 45° with a vibration frequency of 15 Hz, particle agglomeration is substantially reduced. However, frequencies above 18 Hz induce cross-flow recirculation, thereby reducing separation efficiency. Smith et al. [14] employed DEM simulations and high-speed imaging to quantify the impact dehulling dynamics of rice grains. By leveraging the fracture energy difference between rice husks (0.15 J/g) and kernels (0.82 J/g), a multiparameter control model was established, encompassing impact velocity (3–8 m/s), moisture content (12–18%), and collision angle (30°–60°). Under optimized conditions (impact velocity of 6 m/s and 14% moisture content), a dehulling rate of 98.5% with a breakage rate below 2%

was achieved, providing a theoretical benchmark for particle separation based on physical property differences. Markauskas et al. [15] demonstrated that for flexible elongated particles, the nonlinear coupling between particle modulus and airflow velocity significantly affects transport stability, with high-stiffness particles achieving separation efficiencies up to 98% under high airflow conditions. Zhou et al. [16] combined experimental and simulation approaches and found that biomass particles tend to align their long axis along the flow direction in gradient airflow fields. This orientation-enhancing effect markedly improves the effectiveness of shape-based separation. These findings highlight that particle behavior is governed by multifactorial interactions, and effective, stable separation can only be achieved through proper parameter matching and control.

In addition to airflow-related effects, recent DEM-based studies have shown that particle morphology and interface characteristics can significantly influence granular interaction, force transmission, and macroscopic response. For example, Ma et al. [17, 18] reported that particle morphology plays an important role in the shear behavior of granular materials, and further demonstrated that the combined effects of interface roughness and particle shape can substantially alter the mechanical response of granular systems. Although these studies were conducted in granular soil–structure systems rather than gas–solid separators, they provide useful supporting context for understanding why morphology-dependent particle behavior should not be neglected when analyzing the transport and separation of flake-shaped particles. This perspective is particularly relevant to the present study, in which the separated materials exhibit evident non-sphericity.

To further optimize operational parameters in gas–solid separation systems, researchers increasingly rely on numerical simulation methods to systematically uncover flow evolution and particle dynamics. Computational fluid dynamics (CFD), combined with particle modeling approaches such as the discrete phase model (DPM) and discrete element method (DEM), has become a key technical approach for investigating particle separation mechanisms. For example, Sun et al. [19, 20] used CFD–DPM simulations

to examine the influence of inlet structure on flow patterns in air classifiers, demonstrating that proper adjustment of inlet orientation can significantly enhance separation performance. Huang et al. [21] developed an air classifier model with perturbation structures and showed its effectiveness in regulating internal pressure and velocity fields, thereby improving classification efficiency. Zhang et al. [22], through CFD–DEM simulations, found that increasing the rotational speed of moving components enhances particle suspension behavior. Li et al. [23] investigated the coupling between particle size and airflow velocity, revealing their matching principles and impact on separation performance, providing a theoretical basis for controlling particle trajectories. In addition, Su T et al. [24] studied the influence of vortex finder geometry and feed parameters on short-circuit flow in cyclone separators, indicating that reducing vortex finder diameter and increasing wall thickness can suppress short-circuit flow and enhance separation efficiency. However, due to the complexity of model construction and high computational cost, direct reliance on CFD simulations limits comprehensive exploration of the parameter space. Thus, developing high-fidelity predictive models for process optimization is essential for improving the stability and separation performance of air classification systems.

Building upon the mechanistic insights gained through numerical simulations, process parameter optimization is essential for further enhancing system performance. Although artificial neural networks (ANNs) exhibit strong predictive capabilities for complex systems, their reliance on large datasets limits prediction stability when experimental data are scarce [25]. In contrast, response surface methodology (RSM), through design of experiments (DOE), enables the construction of accurate quantitative models between multiple parameters and response indicators. Due to its modeling flexibility and adaptability for optimization, RSM has been extensively applied in engineering optimization tasks [26,27]. The integration of RSM's high-precision modeling capabilities with various multi-objective evolutionary optimization algorithms, such as the multi-objective genetic algorithm (MOGA), non-dominated sorting genetic algorithm (NSGA), and multi-objective particle swarm optimization (MOPSO), has been widely applied in optimizing complex gas–solid separation processes. For example, Tang et al.

[28] combined RSM with a GA–BP neural network model to predict the separation efficiency of a cyclone separator and optimized its structural parameters. Cao et al. [29] employed NSGA-II to optimize the guide vane structure of a cyclone separator, achieving simultaneous improvements in separation efficiency and pressure drop. Li et al. [30] combined CFD–DDPM modeling with multi-objective optimization in a high-speed seed guiding device, enhancing particle transport uniformity and system reliability. Among these algorithms, NSGA-II has notably attracted attention due to its superior optimization performance. Proposed by Deb et al. as an improvement over the original NSGA, NSGA-II introduces a fast non-dominated sorting approach to reduce computational complexity and an elitist preservation strategy to enhance global search capability and solution diversity. These enhancements improve both robustness and convergence speed. Compared to the original NSGA, NSGA-II exhibits superior computational efficiency and global convergence, making it one of the most widely used evolutionary algorithms for multi-objective optimization problems [31].

Furthermore, to facilitate scientific screening and decision-making for Pareto-optimal solutions, the entropy weight method (EWM) combined with the technique for order preference by similarity to ideal solution (TOPSIS) has been widely applied in multi-objective decision-making problems. This method determines the objective weights of evaluation criteria based on information entropy, thereby eliminating subjective bias, and ranks alternatives by computing their distances from the positive and negative ideal solutions, providing high objectivity and broad applicability [32]. For example, Jiang et al. [33] integrated NSGA-II with the EWM-TOPSIS approach for lightweight design of dump truck compartments, enabling comprehensive exploration of the solution space and objective evaluation of alternatives, while balancing structural strength and material utilization. Sun et al. [34] applied NSGA-II and EWM-TOPSIS to optimize an artificial neural network model for wire-cutting process parameters of Ti-6Al-4V alloy, thereby improving process stability and precision control. In the field of heat transfer enhancement, Lv et al. [35] conducted a bi-objective optimization of thermal performance and pressure drop for printed circuit board heat exchangers based

on an RSM–NSGA-II framework, revealing the coupling between key structural parameters and performance responses. Wei et al. [36] employed the RSM–NSGA-III method to optimize the TPMS-fin triple-fluid heat exchanger, achieving a balance between heat transfer efficiency and structural compactness. In summary, the multi-stage framework integrating RSM modeling, NSGA-II optimization, and EWM–TOPSIS decision-making has demonstrated successful applications across various domains. This framework provides a reliable technical approach and theoretical foundation for process parameter optimization in high-concentration particulate systems.

Based on the above, this study proposes a performance-enhancement strategy for a high-concentration particulate separator by integrating the CFD–DDPM (Dense Discrete Phase Model) approach with response surface methodology, NSGA-II optimization, and entropy-weighted TOPSIS decision analysis. It should be emphasized that the novelty of the present work does not lie in the development of a fundamentally new standalone optimization algorithm, but rather in establishing a systematic research route for dense gas–solid separation under practical operating constraints. Compared with previous studies that often focused either on standalone CFD flow analysis or on optimization without sufficiently connecting mechanism interpretation, quantitative prediction, and solution screening, the present study offers three main contributions. First, an experimentally validated CFD-DDPM model was established for the current high-concentration separator, enabling the analysis of dense gas–solid flow behavior and the mechanistic roles of feed velocity, suction pressure, and throwing roller speed. Second, a response-surface-based predictive model was developed to quantitatively characterize the coupled effects of these parameters on particle loss rate and outlet purity. Third, the Pareto-optimal solutions obtained by NSGA-II were further evaluated using entropy-weighted TOPSIS, so that the multi-objective optimization results could be translated into a practically applicable operating condition. In this way, the present work provides not only a parameter optimization route, but also a coherent and validated strategy for simulation, prediction, and operating-condition selection in high-concentration particulate separation.

2. Theory and Methodology

2.1 Physical Model

Given the relatively clear axisymmetric characteristic of the separator geometry and the fact that the dominant gas-solid transport and separation behavior is mainly distributed within a two-dimensional plane, a 2D geometric model was adopted in this study to simplify the full 3D configuration for CFD-DDPM simulation. This simplification not only reduces the computational cost, but also preserves the major flow structures and particle transport features relevant to the present optimization study. As shown in Fig. 1, the simplified model captures the main flow passage, the throwing region, and the outlet separation pathway of the particulate separator, thereby providing an effective basis for parametric simulation, response surface modeling, and multi-objective optimization.

It should be noted that the present 2D model is intended for predicting the main outlet distribution trends and the key separation performance indicators within the operating range considered here. Because it is still a simplified representation of the real separator, more complex three-dimensional local flow non-uniformities, out-of-plane particle interactions, and possible agglomeration behavior under broader operating conditions cannot be fully resolved. The experimental validation of the simplified model is presented in Section 2.5.

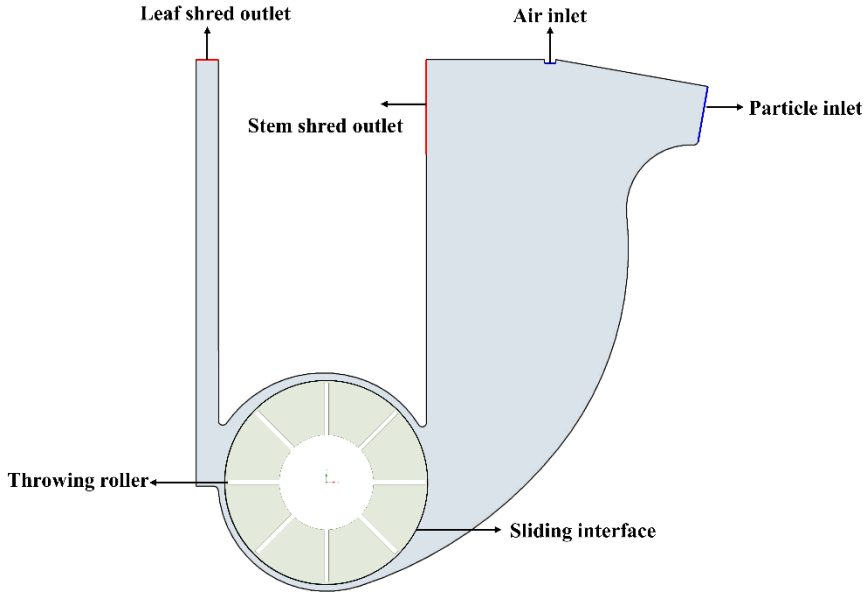

Fig. 1 Model of the particulate separator.

2.2 Mathematical Models and Numerical Methods

2.2.1 Gas-Phase Turbulence Model

Although the geometry of the particulate separator is relatively simple, the internal airflow exhibits highly swirling and anisotropic turbulence. To capture such complex flow features, the SST k–ω turbulence model is employed, as it combines the far-field robustness of the k–ε model with the near-wall accuracy of the k–ω model. This hybrid formulation enables reliable prediction of shear-layer separation and turbulence dissipation in swirling flows. The mathematical formulation and physical interpretation of the SST k-ω model are presented as follows:

Continuity equation:

$$\frac{\partial \rho}{\partial t}+\frac{\partial(\rho u_i)}{\partial x_i}=0 \tag{1}$$

Momentum equation (with turbulent viscosity correction):

$$\frac{\partial(\rho u_i)}{\partial t}+\frac{\partial(\rho u_j u_i)}{\partial x_j}=-\frac{\partial p}{\partial x_i}+\frac{\partial}{\partial x_j}\left[(\mu+\mu_t)\left(\frac{\partial u_i}{\partial x_j}+\frac{\partial u_j}{\partial x_i}\right)\right]+\rho g_i \tag{2}$$

Here, the turbulent viscosity μ_t is constrained by a blending function:

$$\mu_t = \rho \frac{k}{\omega} \cdot min\left(1, \frac{\sqrt{k}}{0.31\omega y}\right) \tag{3}$$

Turbulent kinetic energy (k) equation:

$$\frac{\partial(\rho k)}{\partial t} + \frac{\partial(\rho u_j k)}{\partial x_j} = G_k - \beta^* \rho \omega k + \frac{\partial}{\partial x_j}\left((\mu + \sigma_k \mu_t)\frac{\partial k}{\partial x_j}\right) \tag{4}$$

Where the turbulence production term is given by:

$$G_k = \mu_t \left(\frac{\partial u_i}{\partial x_j} + \frac{\partial u_j}{\partial x_i}\right)\frac{\partial u_i}{\partial x_j} \tag{5}$$

Model constants: $\beta^* = 0.09$

Specific dissipation rate (ω) equation:

$$\frac{\partial(\rho\omega)}{\partial t} + \frac{\partial(\rho u_j \omega)}{\partial x_j} = G_\omega - \beta\rho\omega^2 + \frac{\partial}{\partial x_j}\left((\mu + \sigma_\omega \mu_t)\frac{\partial \omega}{\partial x_j}\right) + D_{k\omega} \tag{6}$$

Production term: $G_\omega = \alpha \frac{\omega}{k} G_k$

Cross-diffusion term: $D_{k\omega} = 2(1 - F_1)\rho\sigma_{\omega 2}\frac{1}{\omega}\frac{\partial k}{\partial x_j}\frac{\partial \omega}{\partial x_j}$

Model constants: $\alpha = 5/9, \beta = 0.075, \sigma_k = 0.85, \sigma_\omega = 0.5$

Blending functions (Shear Stress Transport):

$$F_1 = \tanh\left(min\left(max\left(\frac{\sqrt{k}}{\beta^*\omega y}, \frac{500\nu}{y^2\omega}\right), \frac{4\rho\sigma_{\omega 2} k}{CD_{k\omega} y^2}\right)^4\right) \tag{7}$$

$$F_2 = \tanh\left(max\left(\frac{2\sqrt{k}}{\beta^*\omega y}, \frac{500\nu}{y^2\omega}\right)^2\right) \tag{8}$$

Here, $C = \max\left(2\rho\sigma_{\omega 2}\frac{1}{\omega}\frac{\partial k}{\partial x_j}\frac{\partial \omega}{\partial x_j}, 10^{-10}\right)$

By solving the continuity, momentum, and turbulence transport equations of the SST *k–ω* model, the velocity field, pressure distribution, turbulent kinetic energy (*k*), and specific dissipation rate (*ω*) can be obtained across the separator domain. These quantities are further used to compute eddy viscosity and turbulence intensity, which govern

the development of shear layers, vortex structures, and near-wall flow behaviors. The blending functions ensure a smooth transition between the k–ε and k–ω formulations, enabling robust predictions of both core-flow turbulence and boundary-layer separation. Consequently, the model provides quantitative insights into critical flow characteristics including the recirculation zones, turbulence dissipation, and shear stress distribution, which significantly affects the particle motion and the separation efficiency of the system.

2.2.2 Dense Discrete Phase Model (DDPM)

The conventional Discrete Phase Model (DPM) is based on a one-way coupling assumption, which neglects inter-particle collisions and fragmentation effects. It is applicable only to dilute flows where the solid volume fraction is below approximately 10–12%. However, the high concentration of particles within the particulate separator constitutes a typical dense particulate system. Therefore, this study adopts the Dense Discrete Phase Model (DDPM), which employs a two-way coupling mechanism to simultaneously resolve particle–flow interactions and inter-particle collision dynamics. Compared with DPM, DDPM introduces the concept of "parcels," where clusters of particles are tracked instead of individual particles. This approach significantly reduces computational costs while maintaining acceptable accuracy[37]. Inelastic collisions between particles are quantified using the Kinetic Theory of Granular Flow (KTGF). The granular temperature is used to compute the particle-phase stress tensor, which characterizes momentum transfer and energy dissipation in dense particle clusters[38]. Literature reports[39]indicate that DDPM, by incorporating the interaction of continuous phase, discrete phase, granular stress, and collisions, offers significantly improved predictive accuracy over DPM, particularly in dense flow regimes such as fluidized bed reactors and high-concentration separation systems. The core governing equations are presented below.

Governing equation for particle motion:

The trajectory of a particle parcel is solved using the Lagrangian approach:

$$m_p \frac{d\mathbf{u}_p}{dt} = -\frac{m_p}{\rho_p}\nabla p + \frac{3}{4}\frac{m_p}{\rho_p}\frac{\rho_s}{d_p}C_d \| \mathbf{u}_s - \mathbf{u}_p \|(\mathbf{u}_s - \mathbf{u}_p) + m_p g \frac{\rho_p - \rho_s}{\rho_p} + \mathbf{F}_{\text{KTGF}} \tag{9}$$

Where m_p is the mass of the parcel (kg), d_p is the particle diameter (m), C_d is the drag coefficient (corrected using the Gidaspow model), and $\mathbf{F}_{\text{KTGF}}$ is the inter-particle collision force derived from the gradient of the granular stress tensor:

$$\mathbf{F}_{\text{KTGF}} = \frac{m_p}{\rho_p}\nabla \cdot \sigma_p \tag{10}$$

Granular stress tensor:

The stress tensor of the particle phase σ_p includes pressure and viscous terms:

$$\sigma_p = -p_p \mathbf{I} + \mu_p \left(\nabla \mathbf{u}_p + \nabla \mathbf{u}_p^T\right) + \left(\lambda_p - \frac{2}{3}\mu_p\right)(\nabla \cdot \mathbf{u}_p)\mathbf{I} \tag{11}$$

Where p_p is the granular pressure (Pa), μ_p is the shear viscosity (Pa·s), and λ_p is the bulk viscosity (Pa·s).

The shear viscosity consists of collisional and kinetic contributions:

$$\mu_p = \mu_{p,\text{coll}} + \mu_{p,\text{kin}} \tag{12}$$

$$\mu_{p,\text{coll}} = \frac{4}{5}\alpha_p \rho_p d_p g_0 (1 + e_{pp})\sqrt{\frac{\theta_p}{\pi}} \tag{13}$$

$$\mu_{p,\text{kin}} = \frac{\alpha_p d_p \rho_p \sqrt{\theta_p \pi}}{6(3 - e_{pp})}\left[1 + \frac{2}{5}(1 + e_{pp})(3e_{pp} - 1)\alpha_p g_0\right] \tag{14}$$

$$p_p = \alpha_p \rho_p \theta_p + 2\rho_p (1 + e_{pp})\alpha_p^2 g_0 \theta_p \tag{15}$$

Drag coefficient correction:

For particle volume fractions greater than 0.2, the Gidaspow blended drag model is applied:

$$C_d = \begin{cases} \dfrac{24}{Re_p}(1 + 0.15 Re_p^{0.687}), & \alpha_g \geq 0.8 \\ 150\dfrac{\alpha_p}{\alpha_g Re_p} + 1.75, & \alpha_g < 0.8 \end{cases} \tag{16}$$

where particle Reynolds number $Re_p = \frac{\rho_s d_p \| \mathbf{u}_s - \mathbf{u}_p \|}{\mu_g}$.

By solving the governing equations of the DDPM framework, the velocity, concentration, and stress fields of the particle phase can be simultaneously obtained along with the carrier gas flow field. The granular temperature, derived from KTGF provides a quantitative measure of particle fluctuating energy and serves as the basis for computing granular pressure, shear viscosity and bulk viscosity, which collectively describe momentum transfer and energy dissipation within dense clusters. The corrected drag coefficient (via the Gidaspow model) ensures accurate prediction of interphase momentum exchange under high solid volume fractions. These outputs enable the identification of critical flow features such as particle clustering, collision frequency and segregation patterns, which substantially affect the separation efficiency and the purity. Consequently, the DDPM model allows for the evaluation of key operating parameters such as feed velocity, suction pressure and roller speed by linking them to particle residence time, loss rate, and outlet distribution, providing a reliable basis for optimizing separator performance under dense-flow conditions.

It should be noted that, in the present study, the non-spherical morphology of the flake-shaped particles is incorporated in an approximate engineering manner rather than through a fully orientation-resolved non-spherical particle model. The present DDPM framework combines the Gidaspow blended drag model for interphase momentum exchange with the KTGF-based granular stress formulation for dense-phase collision effects, while the influence of particle non-sphericity is partially reflected through an aspect-ratio-based shape correction factor introduced in the boundary-condition settings. However, no additional dedicated sub-model was implemented to explicitly resolve orientation-dependent drag, lift, or anisotropic contact mechanics for individual flake-shaped particles. Therefore, the present model is suitable for capturing macroscopic transport, outlet distribution, and separation trends within the investigated operating range, but it cannot fully resolve more detailed morphology-dependent particle behaviors.

2.2.3 Numerical Methods

In this study, a two-dimensional model was developed on the ANSYS Fluent 2024R1 platform. The gas-solid two-phase flow was simulated using the Dense Discrete Phase Model (DDPM) within the Euler–Lagrange framework. The governing equations for the continuous phase were the Reynolds-Averaged Navier–Stokes (RANS) equations. The turbulence was modeled using the SST k-ω model, with near-wall treatment handled by standard wall functions. Pressure–velocity coupling was handled using the Phase Coupled SIMPLE algorithm. Both the momentum and turbulence transport equations were discretized using a second-order upwind scheme to enhance the numerical accuracy. The convergence criteria for the CFD-DDPM simulations were defined such that the residuals of the continuity, momentum, and turbulence transport equations were reduced below 1×10^{-6}, ensuring numerical stability and sufficient solution accuracy throughout the computational domain. A gravitational acceleration of 9.81 m/s² was applied in the negative Y-axis direction.

2.3 Boundary Conditions

Continuous phase boundaries: The air inlet was set as a velocity inlet with a magnitude of 5 m/s. The particulate separator outlet was defined as pressure outlets, with a pressure varying from 5000 to 9200 Pa depending on the operating conditions.

Discrete phase boundaries: Two independent injection sources were defined to simulate different particle types in the particulate separation system, with injection directions normal to the inlet surface. The physical properties for the primary particles were: mass flow rate of 0.07595 kg/s, density of 223 kg/m³, and particle diameter of 0.0009 m. For the secondary particles: mass flow rate of 0.00163 kg/s, density of 557 kg/m³, and particle size distribution centered at 0.0032 m. Based on the aspect ratio ($AR = 5.2 \pm 0.8$) of flake-shaped particles, a shape correction factor of 4.97 was adopted from the literature. This treatment, which is consistent with previous DEM-based find-

ings that particle morphology can significantly affect the mechanical and transport behavior of non-spherical granular materials, partially accounts for the effect of non-sphericity on particle motion in the present model. However, orientation-dependent lift and anisotropic contact behavior were not explicitly resolved. Wall–particle collisions were modeled using elastic reflection.The wall roughness was set to 10 μm with a roughness constant of 0.5. In the present model, this roughness parameter mainly affects the near-wall continuous-phase flow through the wall-function treatment, while the particle–wall collision law is separately represented by elastic reflection. A supplementary sensitivity analysis of wall roughness under a representative operating condition is presented in Section 2.6. The effect of turbulent fluctuations on particle dispersion was quantified using the stochastic tracking (random walk) model. A two-way coupling scheme was employed for particle–fluid interactions, with particle trajectories updated every 10 iterations of the continuous phase. This update frequency was validated through a time-step sensitivity analysis to ensure a prediction error of less than 2%.

Rotating components: To capture unsteady effects induced by the rotation of the throwing roller, the sliding mesh approach was used to divide the computational domain into a rotating zone (rotor) and a stationary zone (stator). The rotor region rotated with the throwing roller at an angular velocity of ω = 36–68 rad/s, adjusted according to the operating conditions, while the stator remained stationary. The rotor and stator zones were coupled via a grid-to-grid interface to enable dynamic data exchange, allowing accurate resolution of rotational effects on both the flow field and particle distribution.

2.4 Mesh Independence Verification

To verify mesh independence, the computational mesh for the particulate separation device was generated using the ANSYS MESH tool. A schematic diagram of the mesh configuration is shown in Figure 2. Five mesh configurations with varying densities (3850, 9500, 16,000, 23,000, and 48,000 cells) were constructed, as illustrated in Figure 3. The analysis revealed that increasing the mesh count from 3850 to 23,000 cells led to significant changes in the average mass flow rate at the separator outlet.

However, further increasing the mesh density by approximately 20,000 cells beyond 23,000 resulted in changes of less than 3%, demonstrating convergence of the solution with respect to mesh resolution. Considering computational accuracy, efficiency, and mesh quality (with a minimum orthogonal quality > 0.25), a mesh containing 23,609 cells was selected for all subsequent simulations to balance solution fidelity and computational cost.

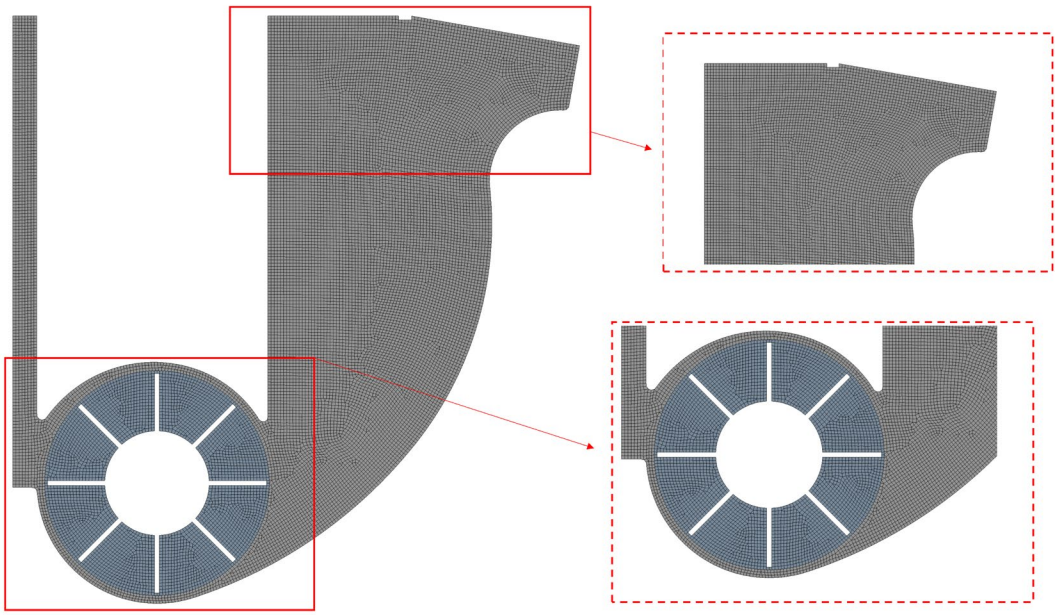

Fig.2 Schematic diagram of mesh discretization.

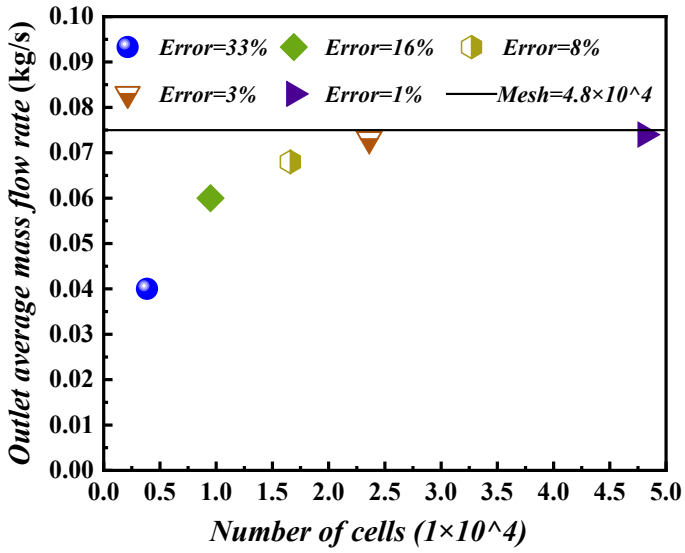

Fig.3 Grid-independent verification.

2.5 Model Validation

To validate the reliability of the 2D CFD-DDPM model in predicting the basic outlet distribution behavior of particles, the simulated mass flow rates at different particle outlets were first compared with experimental measurements under a representative operating condition, namely a feed velocity of 1.28 m/s, a suction pressure of 9200 Pa, and a throwing roller speed of 650 rpm, as shown in Fig. 4. The comparison indicates good agreement between the simulated and measured results in both overall trend and magnitude, demonstrating that the developed numerical model can reasonably capture the particle outlet distribution behavior in the separator.

To further evaluate the predictive capability of the model for the key response indicators used in the optimization study, three representative operating conditions were selected for additional experimental comparison. Case (a) represents a condition with a relatively high particle loss rate, Case (b) represents the condition with optimal separation performance, and Case (c) represents a condition with relatively low outlet purity. For each case, the particle loss rate and outlet purity obtained from the simulations were compared with the corresponding experimental measurements. The validation results are summarized in Tables 1-2 and Figs. 5-6.

For particle loss rate, the relative errors between simulation and experiment for Cases (a)-(c) are 1.83%, 3.34%, and 2.39%, respectively. For outlet purity, the corresponding relative errors are 0.39%, 0.14%, and 0.51%. These results further confirm that the present 2D CFD-DDPM model can not only reproduce the main outlet particle distribution trend, but can also provide reliable predictions for the key separation performance indicators within the investigated operating range.

Although the agreement between simulation and experiment is satisfactory, it should also be emphasized that the present validation is still based on the current separator configuration and selected operating conditions. Therefore, the present model is appropriate for engineering prediction and parameter optimization within the investigated operating range, but its direct application to other particulate systems or substantially different separator geometries should be treated with caution. More specifically,

changes in separator structure, particle properties, inlet–outlet arrangement, or operating regime may alter the dominant gas–solid interaction mechanisms and thus affect model applicability. Nevertheless, for gas–solid separation systems governed by similar physical mechanisms, the integrated methodology adopted in this study, namely CFD-DDPM simulation combined with response surface modeling, NSGA-II optimization, and entropy-weighted TOPSIS decision analysis, can still provide a useful methodological reference. For broader application to other particulate systems or separator geometries, case-specific geometry reconstruction, material-property updating, parameter recalibration, and additional experimental validation would still be required.

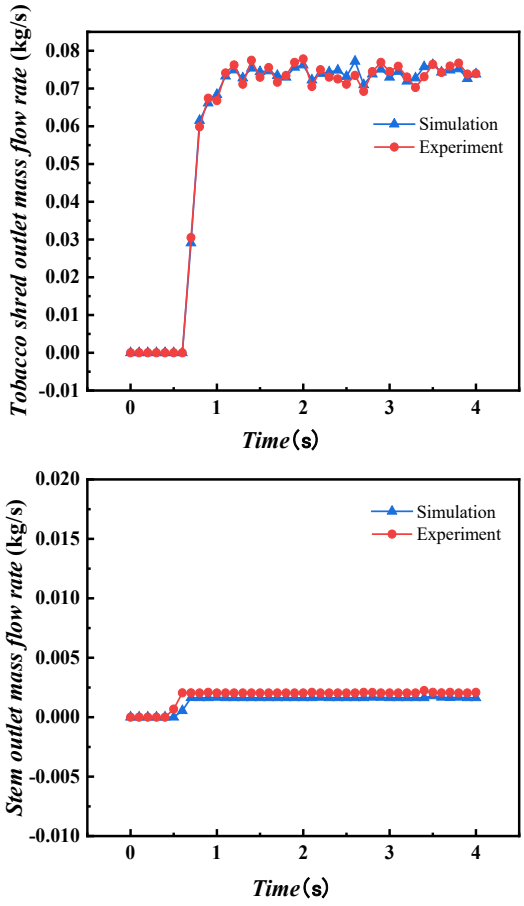

Fig.4 Comparison of experimental data and simulation results.

Table 1. Experimental validation of key response metrics under representative operating Conditions: Particle loss rate

case	Feed velocity (m/s)	Suction pressure (Pa)	Throwing roller speed (rpm)	Particle loss rate -Exp. (%)	Particle loss rate -Sim. (%)	error (%)
Case (a)	1.28	9200	500	1.20	1.1780	1.83

Case (b)	2.00	7100	350	0.32	0.3093	3.34
Case (c)	1.28	5000	500	0.82	0.8004	2.39

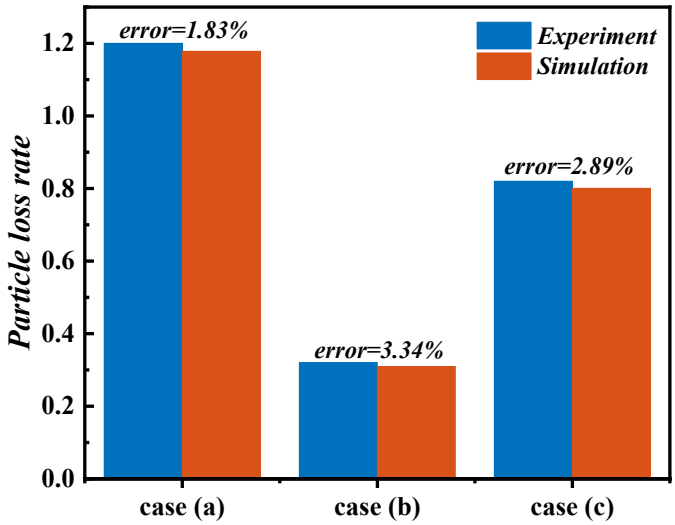

Fig.5. Experimental validation of key response metrics under representative operating Conditions: Particle loss rate

Table 2. Experimental validation of key response metrics under representative operating Conditions: Outlet Purity

case	Feed velocity (m/s)	Suction pressure (Pa)	Throwing roller speed (rpm)	Outlet Purity -Exp. (%)	Outlet Purity -Sim. (%)	error (%)
Case (a)	1.28	9200	500	78.50	78.8093	0.39
Case (b)	2.00	7100	350	99.85	99.9854	0.14
Case (c)	1.28	5000	500	72.50	72.8668	0.51

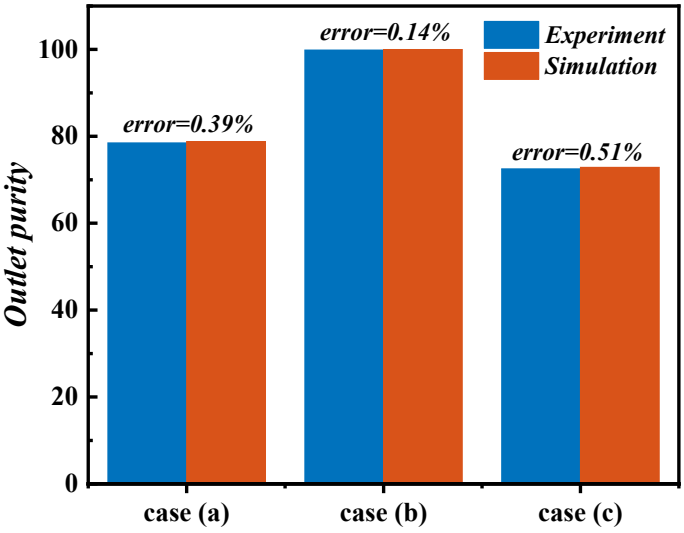

Fig.6. Experimental validation of key response metrics under representative operating Conditions: Outlet Purity

2.6 Sensitivity Analysis of Wall Roughness

A supplementary sensitivity analysis of wall roughness was performed under a representative operating condition corresponding to the optimal separation-performance case, namely a feed velocity of 2.00 m/s, a suction pressure of 7100 Pa, and a throwing roller speed of 350 rpm. Three wall roughness values, 0, 10, and 20 μm, were considered, while the roughness constant was kept at 0.5. The objective of this analysis was to evaluate the influence of wall roughness on the local near-wall flow structure and the global separation performance indicators.

As shown in Fig.7, changes in wall roughness mainly affect the near-wall velocity distribution in the inlet-turning region and along the lower curved wall, whereas the overall mainstream flow pattern in the separator remains broadly similar among the three cases. The enlarged near-wall views further indicate that the local low-velocity structure and velocity gradients adjacent to the wall vary to some extent with increasing wall roughness, suggesting that the roughness parameter primarily influences the continuous-phase flow behavior in the wall-adjacent region.

The corresponding particle-track distributions are shown in Fig.8. It can be observed that variations in wall roughness lead to some differences in the local near-wall particle transport and distribution, especially in the wall-adjacent region highlighted in the enlarged views. However, the overall particle transport paths and outlet tendencies remain generally consistent under the investigated roughness conditions.

The quantitative results are summarized in Table 3. When the wall roughness is changed from 10 μm to 0 and 20 μm, the particle loss rate varies from 0.3093% to 0.3155% and 0.3228%, corresponding to relative deviations of 2.00% and 4.36%, respectively. Under the same conditions, the outlet purity changes from 99.9854% to 99.2315% and 98.5422%, corresponding to relative deviations of 0.75% and 1.44%, respectively. These results indicate that wall roughness mainly exerts a local influence on the near-wall flow field and particle behavior, and has a secondary but non-negligible effect on the global separation metrics within the investigated range. Among the

tested values, the wall roughness of 10 μm provides the best overall separation performance under the representative operating condition. Therefore, the selected value of 10 μm is considered a reasonable engineering choice for the present simulations.

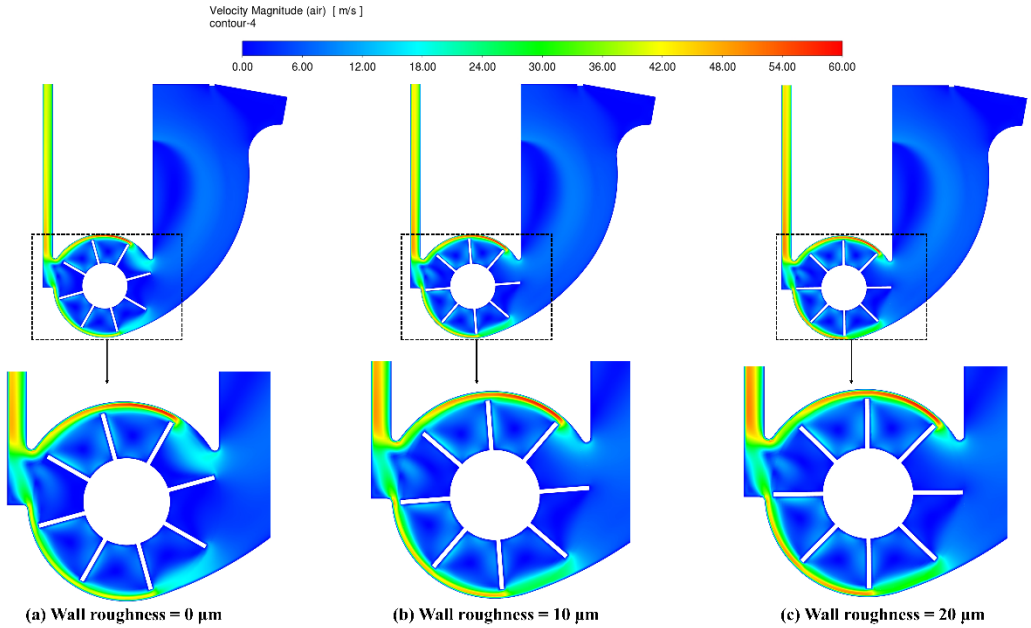

Fig. 7. Velocity magnitude contours under different wall roughness conditions under the representative operating condition: (a) wall roughness = 0 μm, (b) wall roughness = 10 μm, and (c) wall roughness = 20 μm.

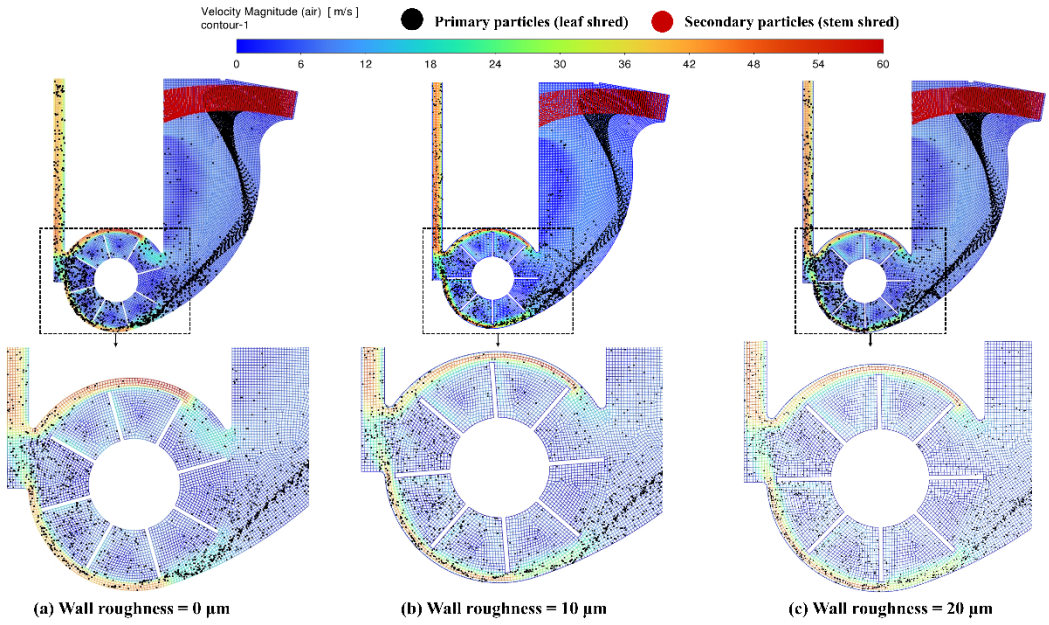

Fig. 8. Particle-track distributions under different wall roughness conditions under the representative operating condition (a) wall roughness = 0 μm, (b) wall roughness = 10 μm, and (c) wall roughness = 20 μm.

Table 3. Sensitivity analysis of wall roughness under a representative operating condition

Wall roughness (μm)	Particle Loss Rate (%)	Relative deviation vs. 10 μm (%)	Outlet Purity (%)	Relative deviation vs. 10 μm (%)
0	0.3155	2.00	99.2315	0.75
10	0.3093	0	99.9854	0
20	0.3228	4.36	98.5422	1.44

2.7 Response Indicators for Performance Evaluation

To comprehensively evaluate the separation performance of the device, this study adopts two response indicators for response surface modeling: particle loss rate and outlet purity. The particle loss rate represents the proportion of target particles that are incorrectly directed to a non-target outlet, reflecting the extent of valuable material loss. In contrast, outlet purity measures the proportion of target particles in the designated outlet, indicating the accuracy of the separation process. These two indicators are complementary and together provide a comprehensive assessment of the device's effectiveness in terms of separation accuracy and misclassification control. The calculation formulas are given in Equations (17) and (18).

The particle loss rate is defined as the proportion of target particles that are misclassified into non-target outlets, and is calculated as follows:

$$L = \frac{N_{leaf\,(stem\ outlet)}}{N_{leaf\,(stem\ outlet)} + N_{stem(stem\ outlet)}} \times 100\% \tag{17}$$

where $N_{leaf\,(stem\ outlet)}$ is the number of target particles misclassified into a non-target outlet, and $N_{stem(stem\ outlet)}$ is the number of correctly separated non-target particles. The denominator represents the total number of particles in the non-target outlet. L denotes the particle loss rate (%), which quantifies the proportion of target particles present in the wrong outlet, reflecting the extent of valuable material loss. A smaller L value indicates a lower degree of mis-separation and improved separation efficiency.

To further assess separation accuracy, the outlet purity indicator is introduced, defined as the proportion of actual target particles in the designated outlet. It is calculated as follows:

$$P = \frac{N_{leaf(leaf\ outlet)}}{N_{leaf(leaf\ outlet)} + N_{stem(leaf\ outlet)}} \times 100\% \tag{18}$$

Where $N_{leaf(leaf\ outlet)}$ is the number of correctly classified target particles, and $N_{stem(leaf\ outlet)}$ is the number of non-target particles misclassified into the target outlet. The denominator represents the total number of particles in the target outlet. P denotes the outlet purity (%), which quantifies the proportion of actual target particles in the outlet. A higher outlet purity (P) indicates greater separation precision and improved overall effectiveness. Together, these complementary indicators provide a comprehensive evaluation of both misclassification control and separation accuracy, forming the basis for subsequent regression modeling and multi-objective optimization of the separator.

2.8 Experimental Design Using Box–Behnken Methodology

To systematically investigate the effects of three factors—feed velocity (A), suction pressure (B), and throwing device speed (C)—on particle loss rate and outlet purity, the Box–Behnken Design (BBD), a method within response surface methodology (RSM), was employed for experimental design. BBD is a commonly used second-order response surface design method, characterized by uniformly distributed design points, high experimental efficiency, and the ability to fit a complete quadratic response model. It is widely applied in the optimization of process parameters.

Each of the three factors was set at three levels, as detailed in Table 4. Based on the principles of BBD, a total of 15 experimental runs were generated, including 3 center points. The detailed design matrix is presented in Table 5.

Table 4. Parameter Level Mapping Table.

Factor	Symbol	−1 (Low)	0 (Medium)	+1 (High)
Feed velocity (m/s)	A	1.28	1.64	2.00
Suction pressure (Pa)	B	5000	7100	9200
Throwing roller speed (rpm)	C	350	500	650

Table 5. Box-Behnken Experimental Design Matrix (15 Runs).

Run	A:Feed velocity	B: Suction pressure	C: Throwing roller speed	Actual A (m/s)	Actual B (Pa)	Actual C (rpm)
1	-1	+1	0	1.28	9200	500
2	+1	+1	0	2.00	9200	500
3	-1	-1	0	1.28	5000	500
4	+1	-1	0	2.00	5000	500
5	-1	0	+1	1.28	7100	650
6	+1	0	+1	2.00	7100	650
7	-1	0	-1	1.28	7100	350
8	+1	0	-1	2.00	7100	350
9	0	+1	+1	1.64	9200	650
10	0	-1	+1	1.64	5000	650
11	0	+1	-1	1.64	9200	350
12	0	-1	-1	1.64	5000	350
13	0	0	0	1.64	7100	500
14	0	0	0	1.64	7100	500
15	0	0	0	1.64	7100	500

Note: Runs 13–15 are repeated center points used to assess model reproducibility and accuracy.

To visually illustrate the spatial structure of the three-factor, three-level Box-Behnken design, Fig. 9 presents the three-dimensional distribution of the design points in normalized space. The three factors—feed velocity, suction pressure, and throwing roller speed—take values within the normalized range of [–1, 0, 1]. The design points are mainly distributed at the edge centers of the factor combinations and at the central point. In the figure, red points indicate edge centers and blue points denote the central point. This design avoids extreme corner points, which enhances simulation stability, improves representativeness of the experimental design, and increases the accuracy of the response surface model fitting.

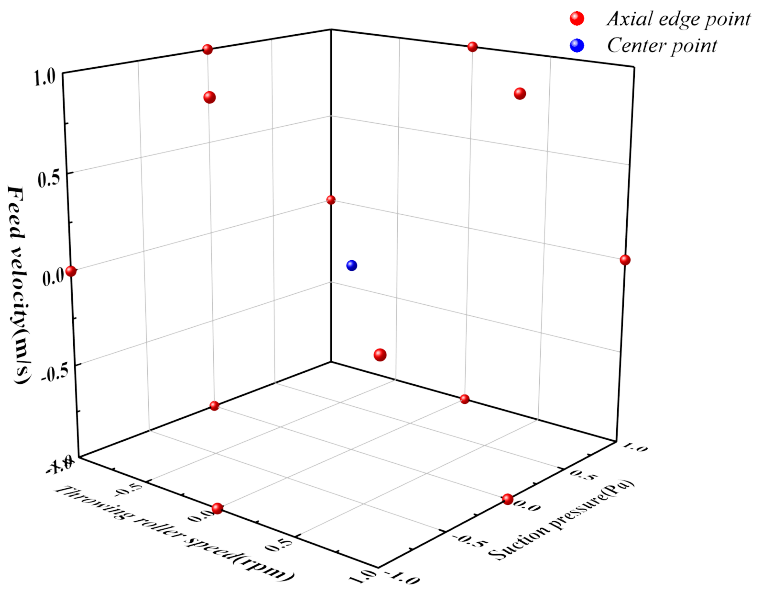

Fig. 9 Distribution of three-factor, three-level Box-Behnken design points.

Based on the Box–Behnken design scheme listed in Table 4, numerical simulations were performed for 15 representative working conditions. For each combination, the type and quantity of particles at the outlets were extracted, and two response metrics including the particle loss rate and the outlet purity were calculated. The corresponding response values for each condition are listed in Table 6.

Table 6. The scheme and results of the Box-Behnken experimental design.

Run	A:Feed velocity	B: Suction pressure	C: Throwing roller speed	Particle loss rate (%)	Outlet purity (%)
1	1.28	9200	500	1.1780	78.8093
2	2.00	9200	500	0.5819	93.3329
3	1.28	5000	500	0.8004	72.8668
4	2.00	5000	500	0.4634	92.6093
5	1.28	7100	650	0.7384	83.5659
6	2.00	7100	650	0.3909	97.9756
7	1.28	7100	350	0.3331	83.9183
8	2.00	7100	350	0.3093	99.9854
9	1.64	9200	650	0.5372	82.9756
10	1.64	5000	650	0.3009	80.9183
11	1.64	9200	350	0.2685	79.9854
12	1.64	5000	350	0.0427	91.6003
13	1.64	7100	500	0.0691	88.8655
14	1.64	7100	500	0.0293	85.6964
15	1.64	7100	500	0.0144	89.7588

3. Results and Analysis

3.1 Analysis of Flow Field Structure and Particle Behavior

To further reveal the separation mechanism under various operating conditions, three representative working cases were selected. These correspond to high particle loss rate (Fig. 10a), optimal separation performance (Fig. 10b), and low outlet purity (Fig. 10c). Detailed analysis of gas–solid flow characteristics was conducted based on the velocity fields and particle trajectories. In Fig. 10, the background contour represents the air-phase velocity magnitude, while the particle tracks of the two particle classes are displayed separately to facilitate direct comparison of their transport paths, segregation characteristics, and outlet tendencies under different operating conditions. Specifically, the black particle tracks represent the primary particles (leaf shred), whereas the red particle tracks represent the secondary particles (stem shred). The revised figure provides a clearer visual basis for distinguishing the transport behavior of the two particle classes under different operating conditions.

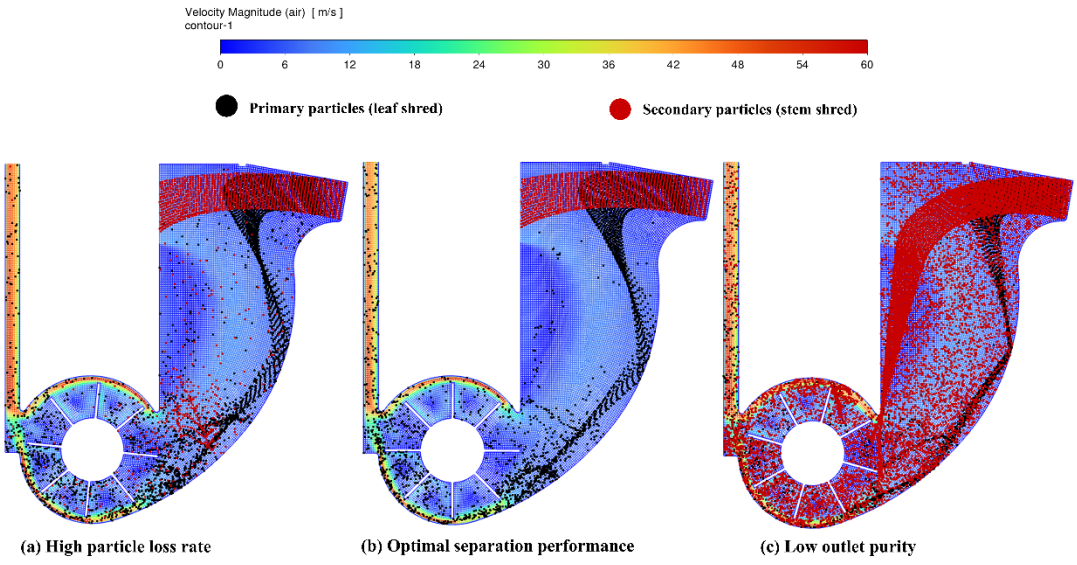

Fig. 10. Velocity contours and particle tracks in the separator under different operating conditions. (a) High particle loss rate: feed velocity = 1.28 m/s, suction pressure = 9200 Pa, and throwing

roller speed = 500 rpm;
(b) Optimal separation performance: feed velocity = 2.00 m/s, suction pressure = 7100 Pa, and throwing roller speed = 350 rpm;
(c) Low outlet purity: feed velocity = 1.28 m/s, suction pressure = 5000 Pa, and throwing roller speed = 500 rpm.

Under the condition shown in Fig. 10(a) (feed velocity: 1.28 m/s, suction pressure: 9200 Pa, throwing device speed: 500 rpm), the system exhibits a high particle loss rate. Although the suction pressure is relatively high, the low feed velocity results in insufficient particle momentum upon entering the separation chamber, making it difficult for the airflow to effectively guide the particles. Moreover, the high rotational speed of the throwing device increases internal airflow disturbances, causing some light particles to deviate from the main flow path. This leads to reverse flow and cross-stream motion, which misguides particles into non-target outlets. Particle trajectories reveal irregular paths of light particles under vortex influence, ultimately contributing to particle loss.

Fig. 10(b) represents the condition with optimal separation performance (feed velocity: 2.00 m/s, suction pressure: 7100 Pa, throwing roller speed: 350 rpm). Under this condition, the internal flow structure is relatively stable, and the moderate-to-high feed velocity ensures sufficient particle momentum, allowing particles to enter the main airflow channel smoothly. The suction pressure is appropriately set to establish a stable directional flow, which effectively guides target particles toward the designated outlet. In addition, the relatively low throwing roller speed suppresses excessive particle dispersion immediately after leaving the roller and weakens the additional local disturbance introduced by the rotating component. This reduces cross-flow mixing inside the separator and helps maintain a clearer separation interface. As a result, stem particles, due to their greater inertia and density, tend to move toward the separation region and are reliably collected, while the entrainment of non-target particles is reduced. The overall gas-solid flow is therefore more organized, with a clearer separation interface and improved separation performance.

The condition in Fig. 10(c) (feed velocity: 1.28 m/s, suction pressure: 5000 Pa, throwing roller speed: 500 rpm) is characterized by low outlet purity. Under this setting,

the initial particle momentum is relatively low, making it difficult to overcome the separation trend caused by inertia differences. Moreover, insufficient suction pressure leads to weak primary airflow induction, resulting in both target and non-target particles following a short and mixed flow path without effective separation. The high throwing device speed induces additional turbulence and airflow recirculation, further disrupting the separation path and increasing particle mixing. Consequently, a significant amount of non-target particles are entrained in the target outlet, markedly reducing the outlet purity.

Comparative analysis of these three representative cases shows that feed velocity, suction pressure, and throwing device speed significantly influence particle momentum transfer, gas–solid interface formation, and separation stability within the system. Achieving optimal separation performance requires a dynamic balance between particle momentum and airflow induction, ensuring effective alignment between high-purity target particle collection and efficient removal of non-target particles.

3.2 Construction and Significance Analysis of the Response Surface Model

To further quantify the influence of process parameters on particle loss rate and outlet purity, and to provide a theoretical basis for optimization design, this study employed the Box–Behnken experimental design to perform multifactor simulation trials on the key influencing variables. Based on the Response Surface Methodology (RSM), regression models were developed. The significance of each factor was examined through analysis of variance (ANOVA), and the interaction patterns among critical parameters were visualized graphically, as detailed below.

3.2.1 Regression Model Development

Regression fitting of the simulation data was performed using Design-Expert 13 software, and quadratic response models were constructed for particle loss rate and outlet purity, respectively. The resulting regression equations are as follows:

$$L = 0.0376 - 0.16305A + 0.119775B + 0.126725C - 0.064775AB - 0.080925AC + 0.002625BC + 0.4369625A^2 + 0.2813625B^2 - 0.0316375C^2 \quad (19)$$

$$P = 88.1069 + 8.0928625A - 0.3614375B - 1.25675C - 1.304725AB - 0.41435AC + 3.41805BC + 1.8945375A^2 - 5.5968625B^2 + 1.3598625C^2 \quad (20)$$

For the particle loss rate model, the coefficient of determination is $R^2 = 0.9724$, and the adjusted R^2 is $R^2_{Adj} = 0.9227$. For the outlet purity model, $R^2 = 0.9397$ and $R^2_{Adj} = 0.8310$. The differences between R^2 and R^2_{adj} in both models are less than 0.2, and the values are close to 1, indicating good model accuracy and high fitting quality. In addition, the Adequate Precision (signal-to-noise ratio) values for the two models are 14.3475 and 10.2497, respectively—both substantially exceeding the threshold of 4—demonstrating strong signal quality and reliable predictive ability. The consistency between the simulation results and the model predictions is high, with minimal deviation. Therefore, the developed RSM models are well-suited for response prediction and process optimization under various operating conditions.

3.2.2 Significance Analysis (ANOVA)

As shown in Fig. 11, residual analysis revealed no outliers, indicating the absence of heteroscedasticity. Fig. 12 demonstrates a strong correlation between predicted and actual values, further confirming the model's reliability and accuracy.

The ANOVA results are presented in Tables 7 and 8. For the particle loss rate model, the F-value is 19.5616 with $P < 0.01$; for the "outlet purity" model, the F-value is 8.65 with $P < 0.05$. These results indicate that both models are statistically significant or highly significant overall. The lack-of-fit P-values for the two models are 0.0574 and 0.2743, respectively, both of which are not significant, indicating that the models are well-fitted and statistically valid.

Further analysis shows that, in the particle loss rate model, feed velocity (A), suction pressure (B), throwing device speed (C), and the quadratic terms A^2 and B^2 have significant effects on the response ($P < 0.05$). The order of influence is: feed velocity > throwing roller speed > suction pressure. In the "outlet purity" model, feed velocity (A) and the quadratic term B^2 are significant ($P < 0.05$), with feed velocity remaining the dominant influencing factor. The interaction term BC shows a noticeable influence, but it does not reach the 0.05 significance level.

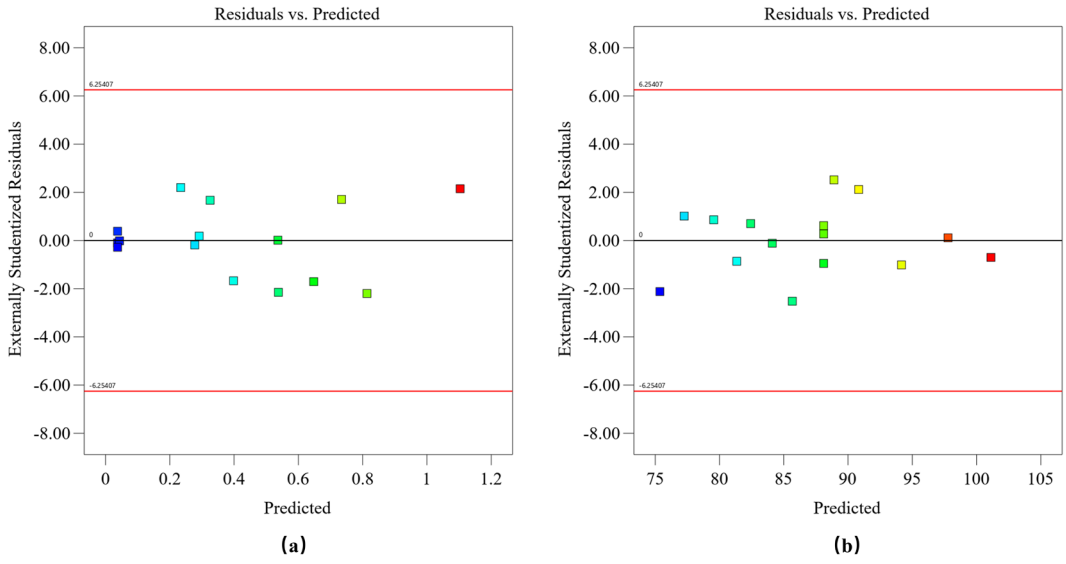

Fig. 11 Residual and fitted values of (a) particle loss rate model, (b) outlet purity model.

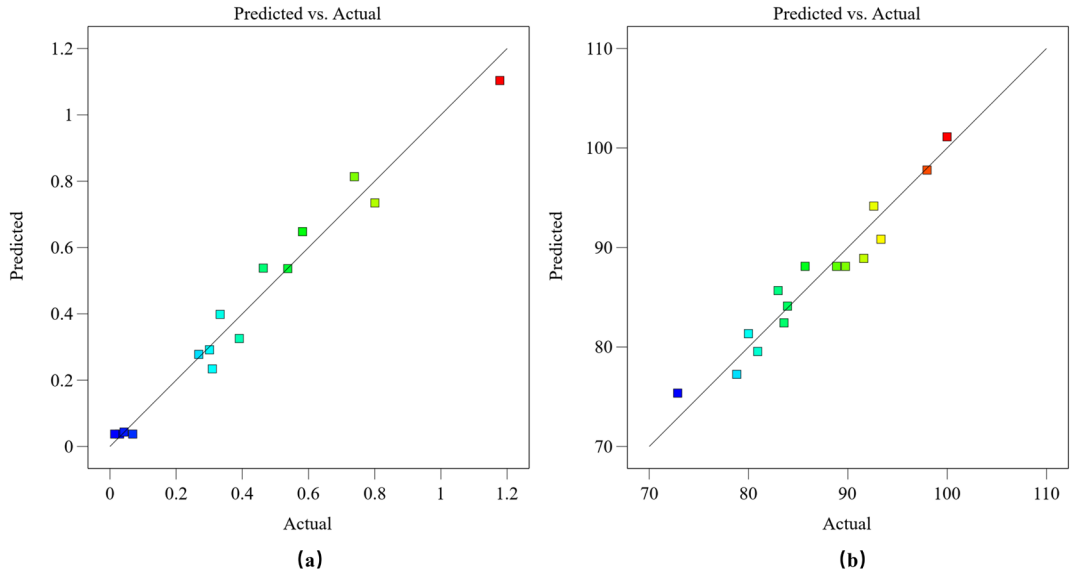

Fig. 12 Comparison of actual and predicted values: (a) particle loss rate model, (b) outlet purity model.

Table.7 Results of the variance analysis (ANOVA) of the particle loss rate model.

Source	Sum of Squares	Degrees of Freedom (DF)	Mean Square	F-Value	P-Value	Signifi-cance
Model	1.4576	9	0.1612	19.5616	0.0022	**
A-Feed ve-locity	0.2127	1	0.2127	25.6886	0.0039	**
B- Suction pressure	0.1148	1	0.1148	13.8622	0.0137	*
C- Throw-ing roller speed	0.1285	1	0.1285	15.5176	0.0110	*
AB	0.0168	1	0.0168	2.0271	0.2138	
AC	0.0262	1	0.0262	3.1640	0.1354	
BC	0.00003	1	0.00003	0.0033	0.9562	
A^2	0.7050	1	0.7050	85.1520	0.0002	**
B^2	0.2923	1	0.2923	35.3052	0.0019	**
C^2	0.0037	1	0.0037	0.4464	0.5337	
Residual	0.0414	5	0.0082			
Lack of Fit	0.0398	3	0.0133	16.5885	0.0574	not signifi-cant
Pure Error	0.0016	2	0.0008			
Cor Total	1.4990	14				

“**” represents highly significant ($P < 0.01$), and “*” represents significant ($0.01 < P < 0.05$).

Table.8 Results of the variance analysis (ANOVA) of the ' outlet purity ' model.

Source	Sum of Squares	Degrees of Freedom (DF)	Mean Square	F-Value	P-Value	Signifi-cance
Model	737.45	9	81.94	8.65	0.0143	*
A-Feed ve-locity	523.96	1	523.96	55.31	0.0007	**
B- Suction pressure	1.05	1	1.05	0.1103	0.7532	
C- Throw-ing roller speed	12.64	1	12.64	1.33	0.3003	
AB	6.81	1	6.81	0.7189	0.4352	
AC	0.6867	1	0.6867	0.0725	0.7985	
BC	46.73	1	46.73	4.93	0.0770	
A^2	13.25	1	13.25	1.40	0.2900	
B^2	115.66	1	115.66	12.21	0.0174	*
C^2	6.83	1	6.83	0.7208	0.4346	
Residual	47.36	5	9.47			

Source	Sum of Squares	Degrees of Freedom (DF)	Mean Square	F-Value	P-Value	Signifi-cance
Lack of Fit	38.25	3	12.75	2.80	0.2743	not signifi-cant
Pure Error	9.11	2	4.56			
Cor Total	784.82	14				

“**” represents highly significant ($P < 0.01$), and “*” represents significant ($0.01 < P < 0.05$).

3.3 Response Surface and Interaction Analysis

3.3.1 Response Surface Analysis of the Particle Loss Rate Model

Based on the developed regression model, three-dimensional response surfaces and contour plots were generated to illustrate the interactive effects of various factors on the particle loss rate, aiming to further elucidate the synergistic influence of key process parameters on system performance.

As shown in Fig. 13, when the throwing device speed is held constant at 500 rpm, the interaction between feed velocity and suction pressure exhibits a distinct non-linear influence on the particle loss rate. As the feed velocity increases, the particle loss rate first decreases significantly, then slightly rises, showing an overall downward trend. In contrast, the effect of suction pressure on the loss rate demonstrates a pattern of initially slow decline followed by a gradual increase, resulting in an overall upward trend. The particle loss rate reaches a relatively minimum value when the feed velocity is 1.64 m/s and the suction pressure is 7100 Pa, indicating optimal separation performance under these conditions.

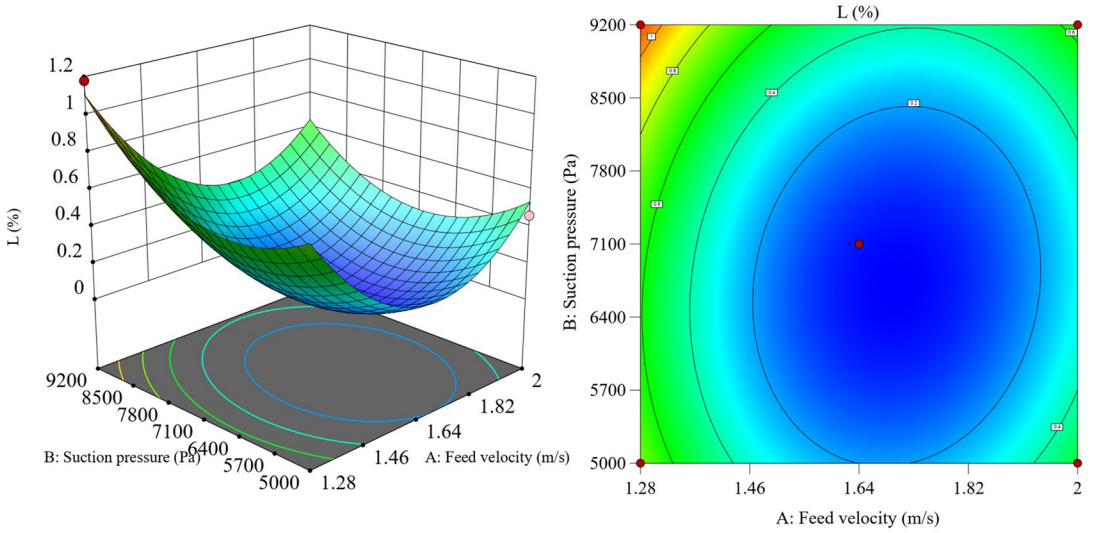

Fig. 13 Response surface and contour plots of the interaction between feed velocity and suction pressure on particle loss rate.

Figure 14 illustrates the interaction between feed velocity and throwing roller speed under a suction pressure of 7100 Pa. The results indicate that the particle loss rate first decreases and then increases with increasing feed velocity, exhibiting a typical "U-shaped" trend. Meanwhile, the loss rate gradually increases with the rise in roller speed, suggesting that higher rotational speeds intensify particle disturbance and elevate the risk of mis-separation. When the feed velocity is 1.64 m/s and the throwing roller speed is 500 rpm, the system similarly achieves an optimal separation state.

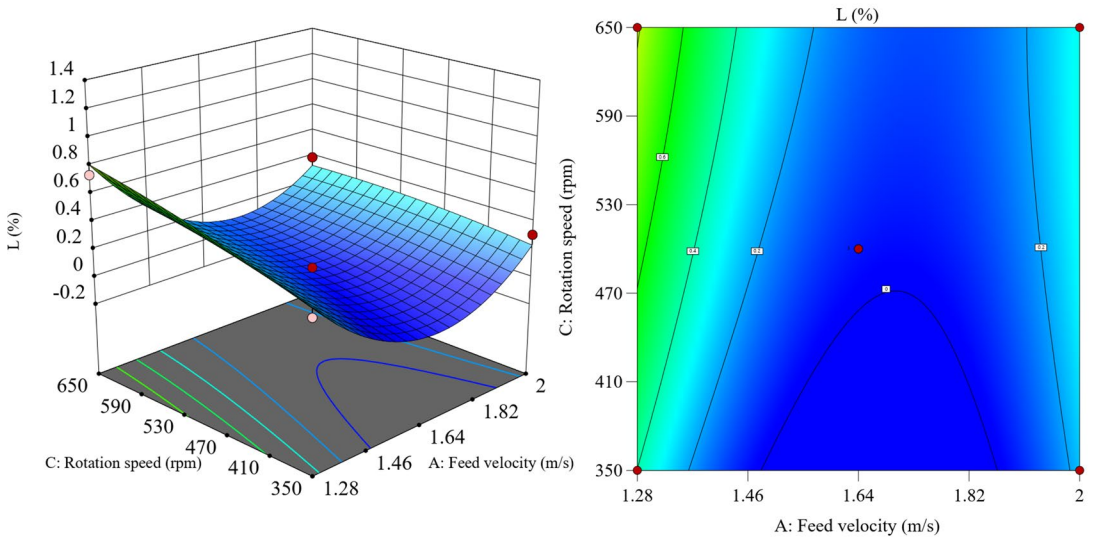

Fig. 14 Response surface and contour plots of the interaction between feed velocity and throwing device speed on particle loss rate.

Figure 15 presents the influence of the interaction between suction pressure and throwing device speed on the particle loss rate at a feed velocity of 1.64 m/s. It can be observed that under lower throwing device speeds, the loss rate first decreases and then levels off with increasing suction pressure, indicating an optimal suction pressure range. However, as the throwing device speed continues to increase, the overall loss rate rises, implying that high speeds disturb the gas–solid separation interface. The minimum particle loss rate is achieved when the suction pressure is 7100 Pa and the throwing device speed is 500 rpm, representing the most favorable operating condition.

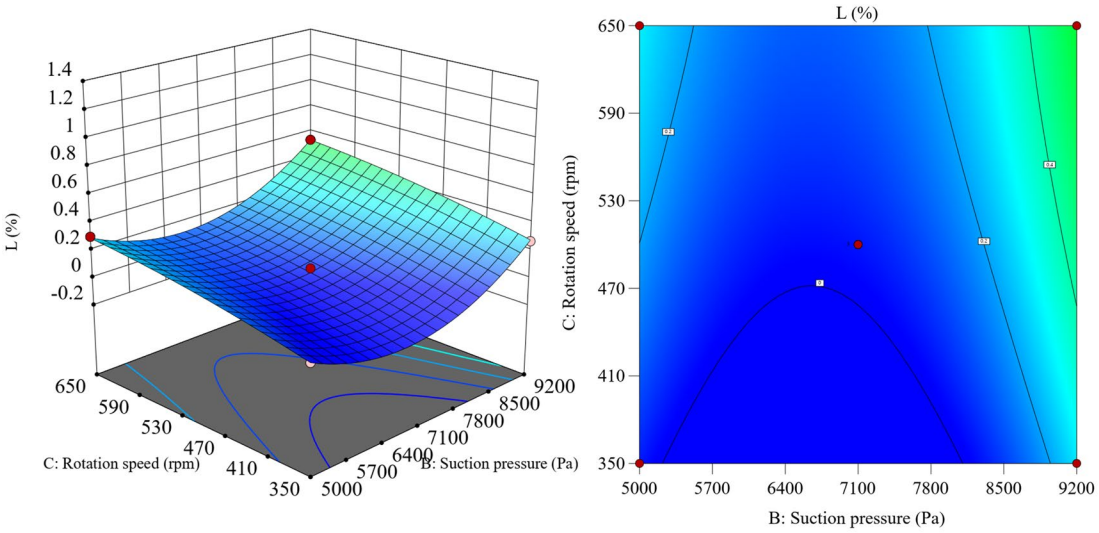

Fig. 15 Response surface and contour plots of the interaction between suction pressure and throwing device speed on particle loss rate.

A comprehensive analysis of the three response surface plots reveals a significant synergistic effect between feed velocity and suction pressure. A well-matched combination ensures sufficient particle momentum while establishing a stable induced airflow, effectively guiding target particles along the desired trajectory. In contrast, the throwing device speed primarily affects the internal airflow structure and the intensity of particle disturbance. A moderate device speed helps maintain the stability of the separation interface, preventing backflow or mis-separation of particles. Therefore, optimizing the combination of feed velocity and suction pressure, while maintaining the device speed

within a reasonable range, is a key strategy to achieve low-loss and high-efficiency separation of target particles.

3.3.2 Response Surface Analysis of the Outlet Purity Model

Based on the established regression equations, three-dimensional response surface plots and contour maps were constructed to analyze how the interactions among various process parameters influence the outlet purity, thereby revealing the coupling effects of key factors on system purity. As shown in Figure 16, when the throwing roller speed is fixed at 500 rpm, the interaction between feed velocity and suction pressure has a notable impact on outlet purity. With the increase in feed velocity, outlet purity consistently improves, indicating that a higher feed rate promotes the directional movement of target particles along the main airflow, thereby reducing impurity entrainment. The variation in suction pressure exhibits a "first increasing, then decreasing" trend, suggesting that a moderate suction strength helps maintain a stable flow field and enhances control over the separation interface. When the feed velocity reaches 2.00 m/s and the suction pressure is 7100 Pa, the outlet purity reaches a relatively high level.

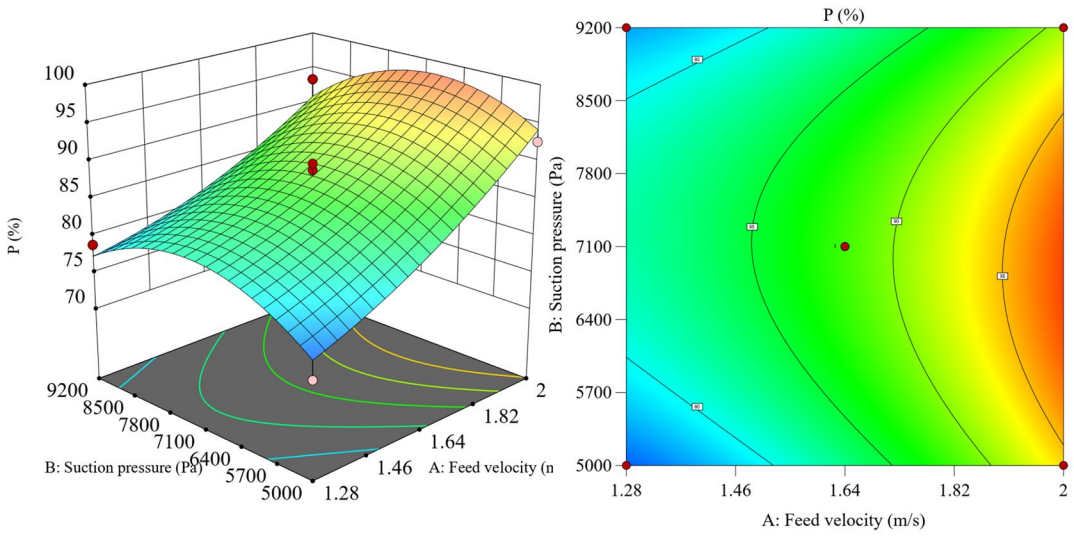

Fig. 16 Response surface and contour plots of the interaction between feed velocity and suction pressure on outlet purity.

Figure 17 illustrates the response surface of outlet purity under the interaction between feed velocity and throwing roller speed, with suction pressure maintained at 7100 Pa. The results show that outlet purity steadily increases with higher feed velocity. In contrast, the effect of roller speed is relatively moderate, exhibiting only a slight upward trend. This suggests that while a higher roller speed may assist in the separation process, it is not the primary determining factor. The optimal outlet purity is achieved when the feed velocity is 2.00 m/s and the throwing roller speed is 500 rpm.

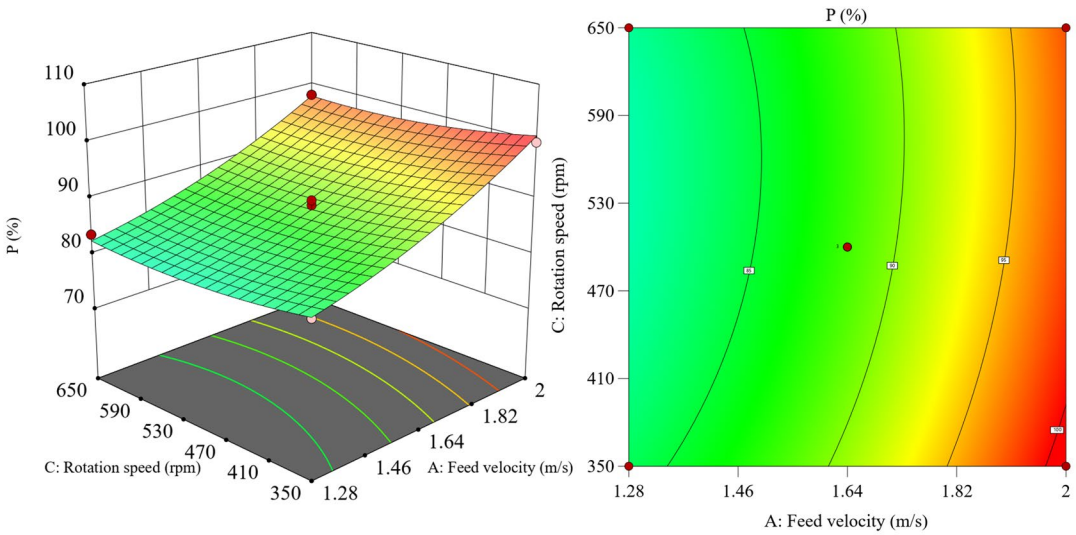

Fig. 17 Response surface and contour plots of the interaction between feed velocity and throwing roller speed on outlet purity.

Figure 18 shows the response surface for the interaction between suction pressure and throwing roller speed on outlet purity at a fixed feed velocity of 1.64 m/s. Overall, outlet purity slightly increases with increasing roller speed, while suction pressure exhibits a "first increasing, then decreasing" trend. This indicates that suction intensity within a critical range can enhance effective separation of target particles, whereas excessive suction may induce backflow or turbulence, compromising separation precision. The optimal outlet purity is observed when suction pressure is 7100 Pa and throwing roller speed is 500 rpm.

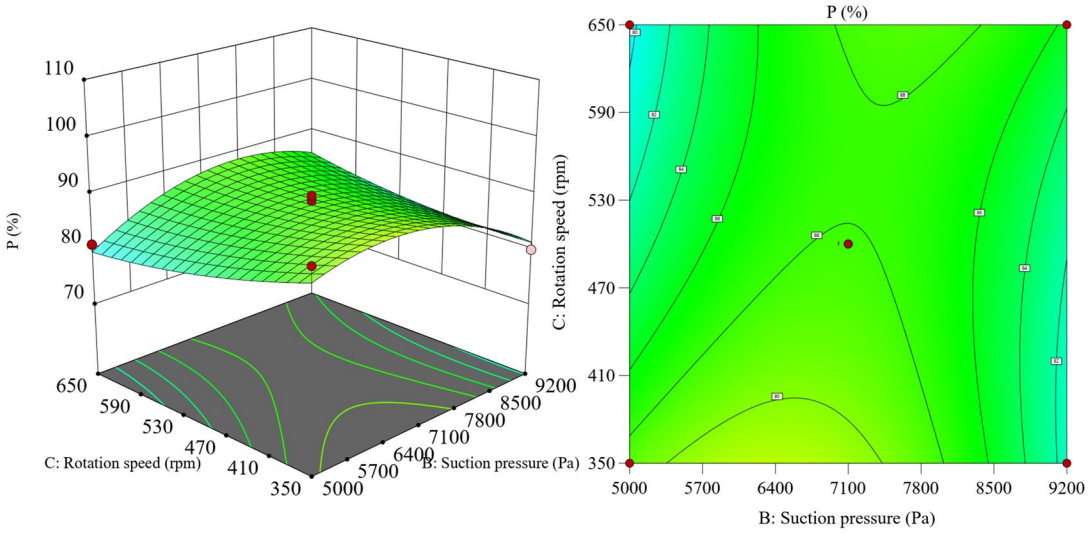

Fig. 18 Response surface and contour plots of the interaction between suction pressure and throwing roller speed on outlet purity.

Based on the analysis of all three response surface plots, feed velocity emerges as the dominant factor influencing outlet purity. Its variation directly determines the momentum conditions for target particles entering the designated path, thereby significantly affecting outlet purity. Although suction pressure and throwing roller speed are not the primary contributors, they play an important synergistic role within specific ranges by stabilizing the internal flow field, guiding particle trajectories, and minimizing misclassification or mixing. Therefore, achieving high outlet purity depends on not only enhancing feed momentum but also appropriately tuning suction intensity and roller speed to optimize particle trajectory distribution and separation interface stability. These findings provide theoretical support and parameter guidance for subsequent multi-objective optimization and separator process control.

Taken together, the response surface results indicate that the optimal operating region is characterized by a relatively high feed velocity, a moderate suction pressure, and a low throwing roller speed. A higher feed velocity within an appropriate range improves the initial momentum of particles and facilitates their entry into the main separation pathway. However, excessively high feed velocity may increase inertial penetration and weaken airflow guidance. Similarly, suction pressure must be high enough

to establish a stable induced airflow field, but excessive suction may intensify local entrainment and disturb the separation interface. By contrast, a lower throwing roller speed is favorable because it reduces additional disturbances introduced by the rotating component, suppresses cross-flow mixing, and helps maintain a clearer and more stable separation interface. This combined trend is consistent with the final optimal parameter combination obtained from the multi-objective optimization.

4. Multi-objective Optimization

4.1 Optimization Process

Figure 19 illustrates the multi-objective optimization workflow employed in this study. First, three key process parameters—feed velocity, suction pressure, and throwing roller speed—were selected as design variables due to their significant influence on separation performance. A Box-Behnken design was applied to perform CFD-DDPM numerical simulations within the defined parameter ranges, and the corresponding response indicators were collected. Based on these results, a second-order regression model was developed using the Response Surface Methodology (RSM) in the form of coded variables.

Analysis of variance (ANOVA) was then performed to evaluate the significance of the regression model, ensuring robust statistical correlation and predictive accuracy. Furthermore, three-dimensional response surface plots were analyzed to investigate the interactions and synergistic effects among the process parameters.

Based on the regression model expressed in terms of actual variables, a multi-objective optimization system was constructed. The Non-dominated Sorting Genetic Algorithm II (NSGA-II) was employed to optimize the objective functions, aiming to simultaneously maximize outlet purity and minimize the particle loss rate. This process yielded a set of Pareto-optimal solutions, reflecting the trade-offs between the competing objectives.

To identify the most favorable parameter combination from the Pareto-optimal solution set, a hybrid decision-making model combining the entropy weight method and TOPSIS was employed. The entropy method objectively determined the weights of each evaluation criterion, while TOPSIS calculated the relative closeness of each solution to the ideal outcome. This approach facilitated the identification of optimal process parameters, providing both theoretical guidance and practical support for controlling the separation system.

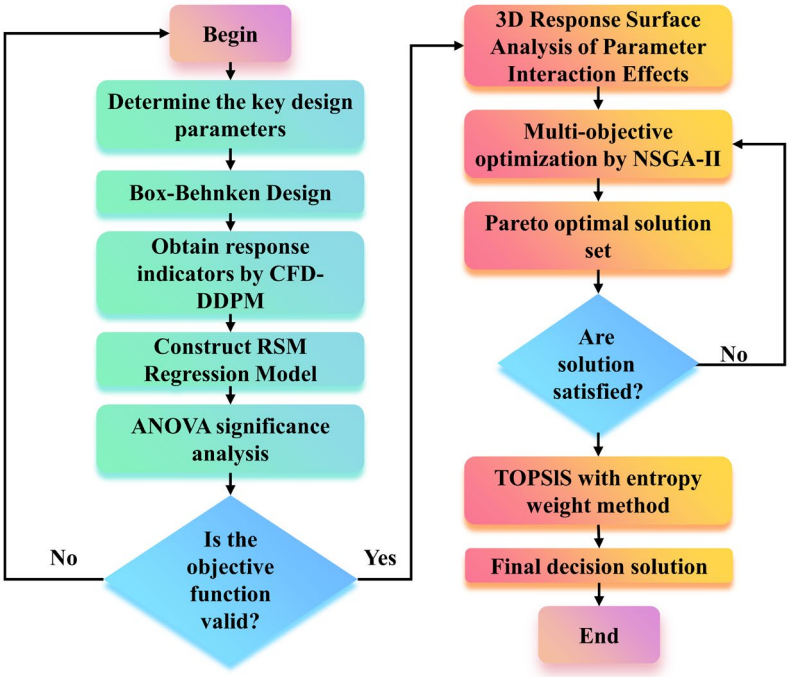

Fig. 19 Flowchart of the multi-objective optimization process.

4.2 Global Optimization via NSGA-II

The NSGA-II optimization process, illustrated in Figure 20, consists of the following six main steps:

(1) The process begins with population initialization, where design variables are sampled using the Latin Hypercube Design method. The objective functions are evaluated via a surrogate model based on Response Surface Methodology (RSM) to reduce computational cost.

(2) Each solution undergoes fast non-dominated sorting and crowding distance calculation to determine its Pareto rank and distribution density.

(3) During the genetic operation phase, binary tournament selection is employed to select parent solutions based on their Pareto rank and crowding distance. The selected parents then undergo Simulated Binary Crossover (SBX, distribution index $\eta_c=15$) and polynomial mutation (probability $p_m=1/dim$) to generate offspring.

(4) The newly generated offspring are evaluated and then combined with the parent population.

(5) The mixed population is trimmed to size N using an elitist selection strategy, and the generation counter is incremented (Gen = Gen + 1).

(6) The loop terminates when one of the following conditions is met: the maximum generation number G_{max} = 500 is reached, or the hypervolume improvement rate remains below 0.1% for 50 consecutive generations. The final Pareto-optimal solution set is then used for decision analysis.

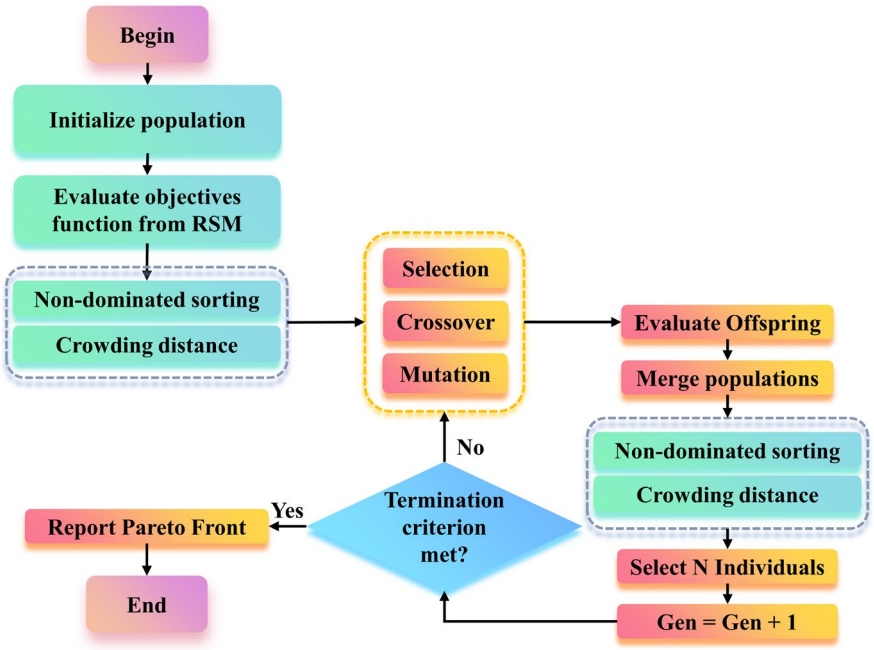

Fig. 20 Flow chart of NSGA-II algorithm

In the response surface modeling phase, all design parameters were normalized to the range of [−1, 1] using coded variables to enhance numerical stability and facilitate visualization of variable interactions. However, for the subsequent NSGA-II-based multi-objective optimization, the regression equations needed to be converted back into their actual-variable form to ensure accurate computation of objective functions within

the real design space. Therefore, the coded variables were transformed into actual variables using standard linear transformation equations before optimization. The actual-variable equations are as follows:

$$\begin{aligned} Y_1 = {} & 9.68907 - 10.15420x_1 - 0.000713x_2 + 0.004649x_3 \\ & -0.000086x_1x_2 - 0.001499x_1x_3 + 8.33333*10^{-9}x_2x_3 \\ & +3.37162x_1^2 + 6.38010*10^{-8}x_2^2 - 1.40611*10^{-6}x_3^2 \end{aligned} \tag{21}$$

$$\begin{aligned} Y_2 = {} & 59.23421 - 9.37805x_1 + 0.015254x_2 - 0.133274x_3 \\ & -0.001726x_1x_2 - 0.007673x_1x_3 + 0.000011x_2x_3 \\ & +14.61834x_1^2 - 1.26913*10^{-6}x_2^2 + 0.000060x_3^2 \end{aligned} \tag{22}$$

In these equations, Y_1 and Y_2 correspond to the actual-variable forms of the coded variables L and P, respectively, while x_1, x_2, and x_3 represent the actual values of the coded variables A, B, and C.

Based on the above regression analysis, the multi-objective optimization problem for the particulate separation process parameters can be formulated as follows:

$$\begin{cases} min\, Y_1 = f_{\text{Loss Rate}}(x_1, x_2, x_3) \\ max\, Y_2 = f_{\text{Outlet Purity}}(x_1, x_2, x_3) \\ s.t. \quad 1.28 \le x_1 \le 2.00 m/s \\ \qquad 7100 \le x_2 \le 9200\text{Pa} \\ \qquad 350 \le x_3 \le 650\text{rpm} \end{cases} \tag{23}$$

The multi-objective optimization model described in Equation (24) was solved using the NSGA-II algorithm implemented in MATLAB. The algorithm parameters were set as follows: an initial population size of 50, a maximum of 500 generations, a crossover probability of 0.9, and a mutation probability of 0.1. The resulting Pareto-optimal front is illustrated in Figure 21. To further examine the distribution characteristics of the Pareto solutions within the design space, Figure 22 illustrates the variation of each design variable among the optimal solutions, providing insights into variable sensitivity and their synergistic trends with respect to the optimization objectives.

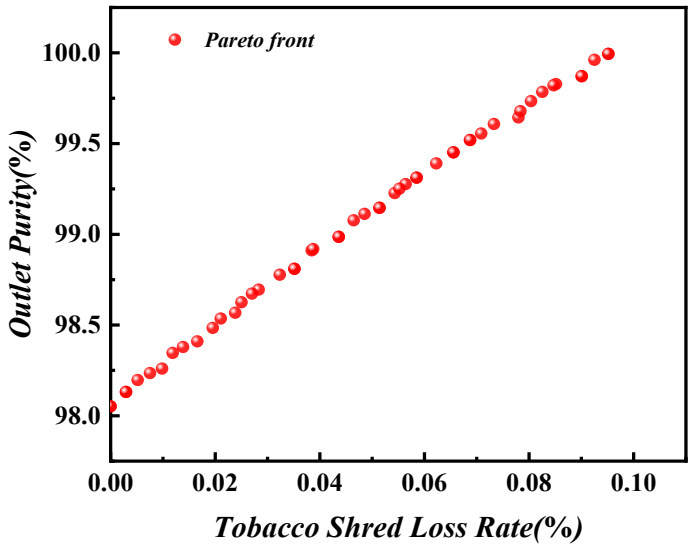

Fig. 21 Pareto Front Diagram.

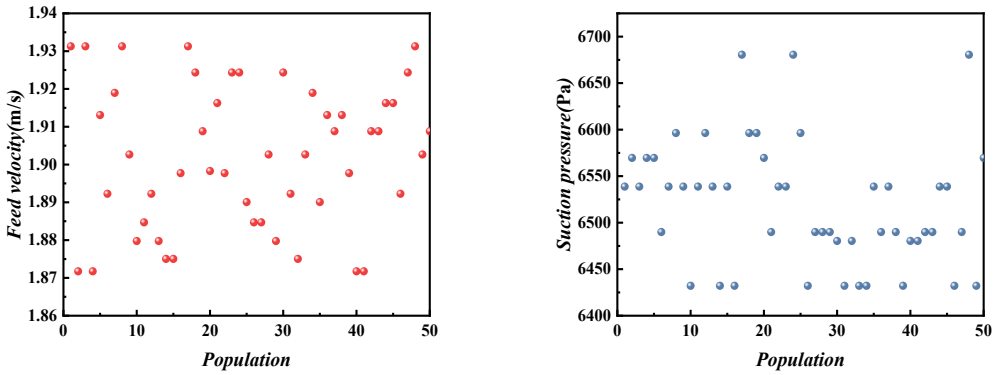

(a) (b)

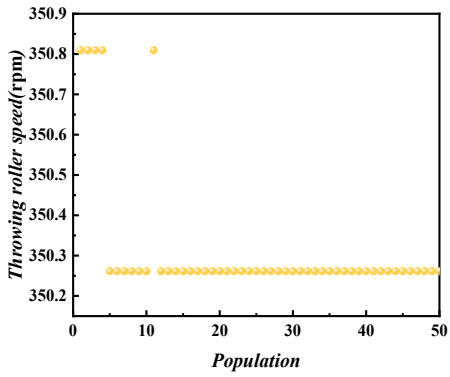

(c)

Fig. 22. Distribution of design variables among the Pareto-optimal solutions.

To verify the distribution characteristics and advantages of the Pareto-optimal solutions, a comparative analysis was conducted, as shown in Fig. 23, against valid samples randomly generated within the feasible domain. In the figure, red dots represent Pareto front solutions obtained via the NSGA-II algorithm based on the response surface model, while black dots correspond to randomly feasible solutions generated through Latin Hypercube Sampling. The comparison indicates that the Pareto solutions provide a superior trade-off between the objective functions Y_1 and Y_2, demonstrating the effectiveness of the optimization algorithm in addressing multi-objective design problems.

From a computational perspective, the dominant cost of the present framework lies in the CFD-DDPM simulations used to generate the response-surface dataset, rather than in the subsequent optimization procedure itself. In the present study, this computational burden was controlled by adopting a two-dimensional model, a parcel-based DDPM formulation, and a Box–Behnken design requiring only 15 representative simulation cases. In addition, a mesh with 23,609 cells was selected as a compromise between computational efficiency and numerical accuracy after mesh-independence verification. After the regression models were established, the NSGA-II search and the subsequent EWM-TOPSIS decision analysis were performed on the surrogate models rather than through repeated direct CFD evaluations. Therefore, compared with a fully CFD-coupled iterative optimization strategy, the additional computational cost of the optimization stage was relatively low. Although the absolute wall-clock time depends on hardware configuration and solver settings, the present modeling–optimization framework provides a computationally feasible approach for engineering-scale parameter optimization. For larger-scale industrial applications or more complex geometries, further efficiency improvement could be achieved through parallel computation and case-specific surrogate updating.

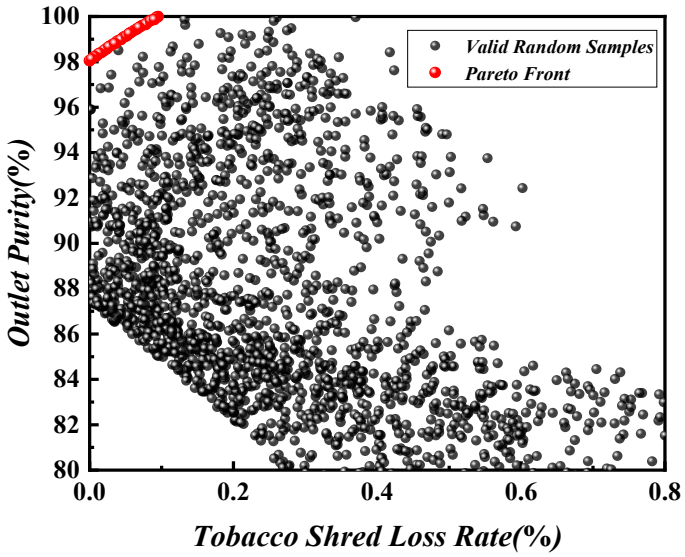

Fig. 23 Comparison between Pareto-optimal solutions and valid random samples.

4.3 Evaluation Method Based on EWM-TOPSIS

To further evaluate and perform decision analysis on the set of Pareto-optimal solutions, a multi-objective evaluation model based on the Entropy Weight Method and Technique for Order Preference by Similarity to Ideal Solution (EWM-TOPSIS) was constructed. This model was used to quantitatively rank 50 representative individuals on the Pareto front (i.e., 50 optimized design schemes) and identify the optimal solution. The entropy weight method is an objective weighting technique based on information entropy theory. It determines the weight of each evaluation criterion according to its variability in the decision matrix, thereby effectively reducing the influence of subjective human bias. The TOPSIS method identifies positive and negative ideal solutions and evaluates each alternative by calculating its Euclidean distance to these ideals. The relative closeness to the ideal solution (closeness coefficient) is then used to rank the quality of the alternatives.

By combining the two methods, the EWM-TOPSIS approach not only reflects the objective influence of each response metric on the target function but also enhances the scientific rigor and accuracy of multi-objective decision-making. The key steps include constructing a dimensionless normalized decision matrix, calculating the entropy and

weight of each criterion, building a weighted normalized matrix, determining the positive and negative ideal solutions, computing the distance from each scheme to the ideal solutions, and calculating the closeness coefficient to identify the optimal design configuration. This method has been widely applied in multi-criteria optimization scenarios due to its strong adaptability and practical effectiveness. The detailed equations are as follows:

(1) Construction of the Original Evaluation Matrix

The evaluation indicators of 50 optimal ratio schemes from the Pareto front are defined as the original evaluation matrix, expressed as:

$$\mathbf{A} = [a_{ij}]_{50\times 2} \quad (i = 1,...,50; j = 1,2) \tag{24}$$

Where $\mathbf{A}$ is the original evaluation matrix, and a_{ij} represents the value of the j-th evaluation indicator for the i-th optimization scheme.

(2) Normalization

The matrix $\mathbf{A}$ is dimensionlessly normalized to scale all indicators. The normalization formulas for different types of indicators (where outlet purity is a positive indicator and particle loss rate is a negative indicator) are shown in Equations (26) and (27), respectively.

Positive indicator:

$$b_{i1} = \frac{a_{i1} - \min\limits_{k} a_{k1}}{\max\limits_{k} a_{k1} - \min\limits_{k} a_{k1}} \tag{25}$$

Negative indicator:

$$b_{i2} = \frac{\max\limits_{k} a_{k2} - a_{i2}}{\max\limits_{k} a_{k2} - \min\limits_{k} a_{k2}} \tag{26}$$

The resulting normalized matrix is denoted as $\mathbf{B} = [b_{ij}]_{50\times 2}$

(3) Determination of Entropy Weights of Evaluation Indicators

$$p_{ij} = \frac{b_{ij}}{\sum\limits_{i=1}^{50} b_{ij}} \tag{27}$$

$$e_j = -\frac{1}{\ln 50} \sum_{i=1}^{50} p_{ij} \ln p_{ij} \tag{28}$$

$$w_j = \frac{1-e_j}{\sum_{j=1}^{2}(1-e_j)} \tag{29}$$

The objective weights of each evaluation indicator in the Pareto front are calculated. The results are shown in Table 9.

Table 9 Information entropy and entropy weight of each evaluation index

Evaluation indicator	Information entropy	Entropy weight
Y_1(L)	0.99475	0.50644
Y_2(P)	0.99488	0.49356

(4) Construction of the Weighted Decision Matrix

$$c_{ij} = w_j \times b_{ij} \tag{30}$$

The weighted decision matrix is denoted as $\mathbf{C} = [c_{ij}]_{50\times 2}$

(5) Determination of the Positive and Negative Ideal Solutions

$$\mathbf{C}^{+} = \left(\max_i c_{i1}, \max_i c_{i2}\right) \tag{31}$$

$$\mathbf{C}^{-} = \left(\min_i c_{i1}, \min_i c_{i2}\right) \tag{32}$$

(6) Calculation of Euclidean Distances from Each Scheme to the Positive and Negative Ideal Solutions

$$D_i^{+} = \sqrt{(c_{i1}-c_1^{+})^2 + (c_{i2}-c_2^{+})^2} \tag{33}$$

$$D_i^{-} = \sqrt{(c_{i1}-c_1^{-})^2 + (c_{i2}-c_2^{-})^2} \tag{34}$$

(7) Calculation of the Relative Closeness Coefficient

$$C_i = \frac{D_i^{-}}{D_i^{+} + D_i^{-}} \tag{35}$$

Where C_i is the relative closeness coefficient of the *i*-th optimization scheme. A value closer to 1 indicates a better overall evaluation performance.

(8) Selection of the Optimal Solution

$$\text{Optimal solution} = \arg \max_{1\le i\le 50} C_i \tag{36}$$

To evaluate the overall performance of each solution, the relative closeness of the Pareto optimal solutions to the ideal solution was calculated, as shown in Fig. 24. This

closeness coefficient comprehensively considers both the particle loss rate and outlet purity, objectively reflecting how close each solution is to the ideal one. As illustrated in Fig. 24, Solution 22 exhibits the highest closeness coefficient and is the nearest to the ideal solution, indicating superior overall performance. Therefore, it is selected as the optimal operational scheme. Fig. 25 depicts the location of this optimal solution on the Pareto front. Under these operating conditions, the particle loss rate (L) is 0.0387%, the outlet purity (P) is 98.9189%, and the corresponding design parameters are a feed velocity of 1.89 m/s, suction pressure of 6539 Pa, and throwing device speed of 350 rpm.

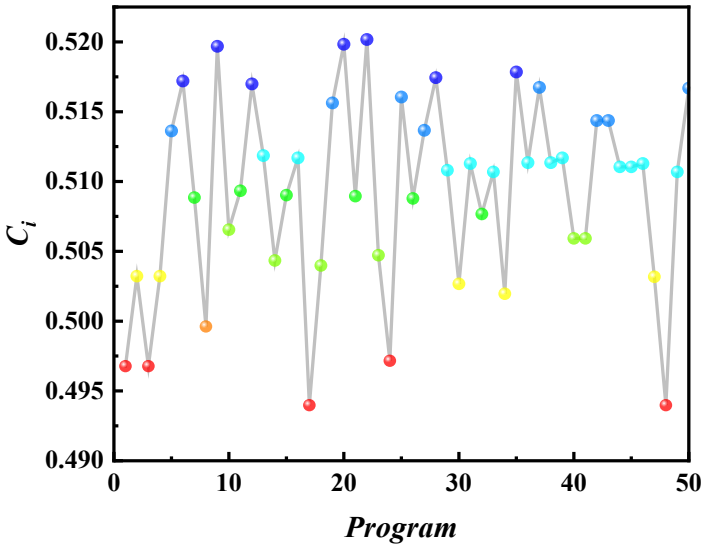

Fig. 24 Relative closeness of each program.

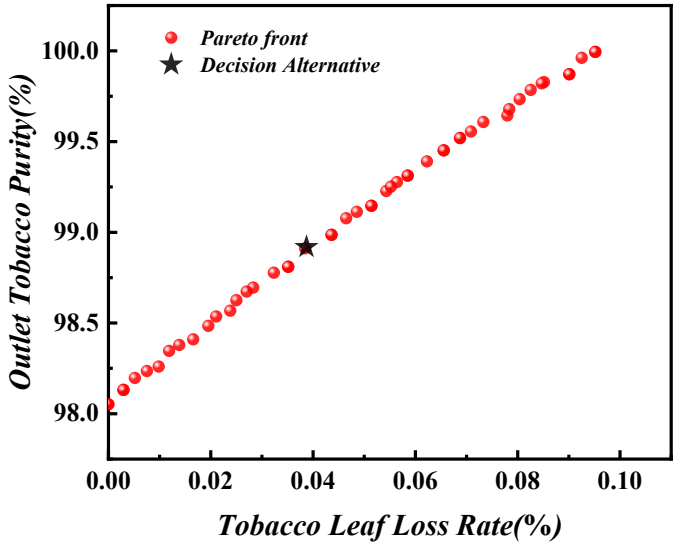

Fig. 25 Decision alternative.

To validate the accuracy of the optimization model, a numerical simulation was conducted under the optimal operating conditions, and the results were compared with the predicted values. As shown in Table 10 and Figure 26, the relative errors for the particle loss rate and outlet purity were 1.808% and 0.314%, respectively, validating the reliability and practical applicability of both the regression model and the optimization method.

Table 10. Optimization Results Validation.

Test Conditions	X_1（m/s）	X_2（Pa）	X_3（rpm）	Y_1（particulate loss rate /%）	Y_2（Outlet Purity/%）
Predicted	1.89	6539	350	0.0387	98.9189
Simulated	1.89	6539	350	0.0394	98.6093
Relative Error/%				1.808	0.314

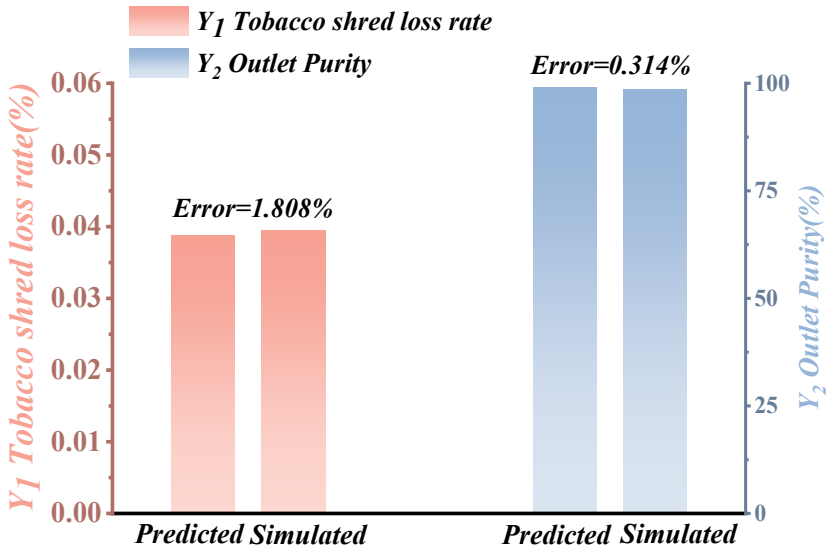

Fig. 26 Comparison of predicted and simulated results with relative errors.

A comprehensive analysis indicates that the optimized parameter combination corresponds to a balanced operating state located within the favorable region identified by the response surface analysis, namely a relatively high feed velocity, a moderate suction pressure, and a low throwing roller speed. Specifically, the feed velocity of 1.89 m/s provides sufficient initial momentum for particles to enter the main separation pathway, while avoiding excessive inertial penetration that would weaken the guidance effect of

the airflow and increase the risk of misclassification. The suction pressure of 6539 Pa helps establish a stable directional induced airflow field, which enhances selective particle transport and maintains a clearer separation interface, while avoiding the excessive entrainment that may occur at higher suction levels. Meanwhile, the relatively low throwing roller speed of 350 rpm suppresses excessive particle dispersion immediately after leaving the roller, weakens the additional local disturbance introduced by the rotating component, and reduces cross-flow mixing inside the separator. Within the DDPM framework, these combined effects improve particle transport stability, reduce non-target entrainment, and help maintain a clearer gas–solid separation interface. As a result, the optimized condition simultaneously achieves a very low particle loss rate and a high outlet purity.

5. Conclusions

Based on the CFD-DDPM gas–solid two-phase flow model and multi-objective optimization framework, this study systematically analyzed flow field characteristics and particle separation behavior within a high-concentration particulate separation system. The key findings are summarized as follows:

(1) The developed SST k-ω turbulence model combined with the Dense Discrete Phase Model (DDPM) accurately captured the gas–solid flow characteristics within the separator. Experimental validation showed an error margin within 5.0%, confirming the model's capability in predicting both particle trajectories and flow structures.

(2) A total of 15 simulation runs were conducted based on the Box–Behnken design, yielding two quadratic regression response surface models. The coefficients of determination (R^2) were 0.9724 and 0.9397, and the adjusted R^2 values were 0.9227 and 0.8310, respectively—both close to 1. The adequate pre-

cision ratios were significantly higher than the threshold values, and the prediction errors remained within acceptable limits, indicating the models' suitability for optimization and operating condition forecasting.

(3) Analysis of main and interaction effects showed that feed velocity, suction pressure, and throwing roller speed jointly influence particle loss rate and outlet purity, with feed velocity being the dominant factor for both responses. For outlet purity, feed velocity and the quadratic effect of suction pressure were identified as the major statistically significant terms, whereas the interaction between suction pressure and throwing roller speed played a secondary role within the investigated range.

(4) A multi-objective optimization problem was formulated using regression models based on actual variables. The Non-dominated Sorting Genetic Algorithm II (NSGA-II) was employed to simultaneously minimize particle loss rate and maximize outlet purity. A set of Pareto-optimal solutions representing different trade-offs was obtained, and their distribution and evolutionary characteristics within the design variable space were analyzed.

(5) A comprehensive evaluation and ranking of 50 Pareto-optimal solutions were conducted using the entropy weight method combined with the TOPSIS approach. The optimal operating parameters were identified as a feed velocity of 1.89 m/s, suction pressure of 6539 Pa, and throwing device speed of 350 rpm, corresponding to predicted values of a particle loss rate of 0.0387% and an outlet purity of 98.9189%, indicating the best overall performance. Validation simulations confirmed errors below 5%, verifying the reliability of the model for parameter selection and separator performance improvement.

Acknowledgements

This work was financially supported by The Key R&D Program of Henan Province (241111320900), The Central Government Guided Local Science & Technology Development Fund of Henan Province (Z20241471018), The Science & Technology Tackling Program of Henan Province (252102320163) and R&D Project of Anyang Cigarette Factory, China Tobacco Henan Industrial Co., Ltd. (AYBW202406).

References

[1] Y. Liu, C. Xin, J. Tang, S. Xu, Y. Yin, CFD-DEM simulation and experimental validation of air classification for tobacco particles, Powder Technology, 448 (2024) 120318. https://doi.org/10.1016/j.powtec.2024.120318.

[2] Q. Luo, X. Huang, J. Wu, X. Mou, Y. Xu, S. Li, G. Ma, F. Wan, L. Peng, Simulation Analysis and Parameter Optimization of Seed-Flesh Separation Process of Seed Melon Crushing and Seed Extraction Separator Based on DEM, Agriculture-Basel, 14 (2024) 1008. https://doi.org/10.3390/agriculture14071008.

[3] Z. Zhen, H. Zhang, O. Zhang, B. Li, Z. Zhang, Effect of drill hole inclination on coal particles-gas flow characteristics in negative pressure sampling process, Powder Technology, 450 (2025) 120447. https://doi.org/10.1016/j.powtec.2024.120447.

[4] P. Chen, Y. Han, F. Jia, D. Zhao, X. Meng, A. Li, Y. Chu, H. Zhao, Investigation of the mechanism of aerodynamic separation of rice husks from brown rice following paddy hulling by coupled CFD-DEM, Biosystems Engineering, 218 (2022) 200-215. https://doi.org/10.1016/j.biosystemseng.2022.03.015.

[5] S. Yuan, G. Sun, G. Cao, Y. Wu, Y. Yue, Z. Song, Study of the performance and flow field of a new spiral-roof cyclone separator, Powder Technology, 438 (2024) 119605. https://doi.org/10.1016/j.powtec.2024.119605.

[6] B. Sun, X. Che, F. Wu, J. Hao, X. Li, The performance research of airflow multistage spouted bed by experimental and simulative methods, Powder Technology, 453 (2025) 120631. https://doi.org/10.1016/j.powtec.2025.120631.

[7] Y. Zhang, K. Li, K. Zhang, G. Zhu, Z. Sun, J. Shi, Research on the Flow Field Characteristics of the Industrial Elliptical Cyclone Separator, Separations, 12 (2025) 50. https://doi.org/10.3390/separations12020050.

[8] M. Mirzaei, P.A. Jensen, M. Nakhaei, H. Wu, S. Zakrzewski, H. Zhou, W. Lin, A hybrid multiphase model accounting for particle agglomeration for coarse-grid simulation of dense solid flow inside large-scale cyclones, Powder Technology, 399 (2022) 117186. https://doi.org/10.1016/j.powtec.2022.117186.

[9] C.W. Haig, A. Hursthouse, S. McIlwain, D. Sykes, The effect of particle agglomeration and attrition on the separation efficiency of a Stairmand cyclone, Powder Technology, 258 (2014) 110-124. https://doi.org/10.1016/j.powtec.2014.03.008.

[10] H.A. Petit, E.F. Irassar, The throat classifier: A novel air classifier for the control of dust in manufactured sands, Powder Technology, 390 (2021) 417-427. https://doi.org/10.1016/j.powtec.2021.05.049.

[11] H. Zhao, Y. Zhao, CFD-DEM simulation of pneumatic conveying n a horizontal pipe, Powder Technology, 373 (2020) 58-72. https://doi.org/10.1016/j.powtec.2020.06.054.

[12] S. Chakravarty, M. Fischer, P. Garcia-Trinanes, D. Parker, O. Le Bihan, M. Morgeneyer, Study of the particle motion induced by a vortex shaker, Powder Technology, 322 (2017) 54-64. https://doi.org/10.1016/j.powtec.2017.08.026.

[13] M. Fischer, S. Chakravarty, O. Le Bihan, M. Morgeneyer, Parametric study of the particle motion induced by a vortex shaker, Powder Technology, 374 (2020) 70-81. https://doi.org/10.1016/j.powtec.2020.06.060.

[14] Y. Chu, Y. Han, F. Jia, Y. Wang, P. Chen, X. Meng, J. Zhang, A. Li, Analysis of the impact hulling behaviour of paddy grains, Biosystems Engineering, 220 (2022) 243-257. https://doi.org/10.1016/j.biosystemseng.2022.06.005.
[15] D. Markauskas, S. Platzk, H. Kruggel-Emden, Comparative numerical study of pneumatic conveying of flexible elongated particles through a pipe bend by DEM-CFD, Powder Technology, 399 (2022) 117170. https://doi.org/10.1016/j.powtec.2022.117170.
[16] C. Zhou, H. Chen, J. Su, Y. Chen, Orientation simulation and image experiment for flexible biomass particle in wedge fluidization channel, Journal of Food Engineering, 333 (2022) 111150. https://doi.org/10.1016/j.jfoodeng.2022.111150.
[17] X. Ma, H. Lei, X. Kang, Examination of interface roughness and particle morphology on granular soil–structure shearing behavior using DEM and 3D printing, Engineering Structures, 290 (2023) 116365. https://doi.org/10.1016/j.engstruct.2023.116365.
[18] X. Ma, H. Lei, X. Kang, Effects of particle morphology on the shear response of granular soils by discrete element method and 3D printing technology, International Journal for Numerical and Analytical Methods in Geomechanics, 46 (2022) 2191–2208.https://doi.org/10.1002/nag.3384.
[19] Z. Sun, L. Liang, C. Liu, Y. Zhu, L. Zhang, G. Yang, CFD simulation and performance optimization of a new horizontal turbo air classifier, Advanced Powder Technology, 32 (2021) 977-986. https://doi.org/10.1016/j.apt.2021.01.041.
[20] Z. Sun, G. Sun, J. Liu, X. Yang, CFD simulation and optimization of the flow field in horizontal turbo air classifiers, Advanced Powder Technology, 28 (2017) 1474-1485. https://doi.org/10.1016/j.apt.2017.03.016.
[21] L. Huang, J. Yuan, M. Pan, J. Wu, J. Qiao, H. Jiang, C. Duan, CFD simulation and parameter optimization of the internal flow field of a disturbed air cyclone centrifugal classifier, Separation and Purification Technology, 307 (2023) 122760. https://doi.org/10.1016/j.seppur.2022.122760.
[22] H. Zhang, O. Zhang, B. Li, J. Zhang, X. Xu, J. Wei, Effect of drill pipe rotation on gas-solid flow characteristics of negative pressure pneumatic conveying using CFD-DEM simulation, Powder Technology, 387 (2021) 48-60. https://doi.org/10.1016/j.powtec.2021.04.017.
[23] B. Li, H. Zhang, J. Wei, O. Zhang, Y. Guo, J. Zhang, L. Si, X. Xu, Coal particle transport behavior in a rotating drill pipe used for negative pressure pneumatic conveying, Powder Technology, 402 (2022) 117369. https://doi.org/10.1016/j.powtec.2022.117369.
[24] T. Su, Y. Zhang, Effect of the Vortex Finder and Feed Parameters on the Short-Circuit Flow and Separation Performance of a Hydrocyclone, Processes, 10 (2022) 771. https://doi.org/10.3390/pr10040771.
[25] I. Veza, M. Spraggon, I.M.R. Fattah, M. Idris, Response surface methodology (RSM) for optimizing engine performance and emissions fueled with biofuel: Review of RSM for sustainability energy transition, Results in Engineering, 18 (2023) 101213. https://doi.org/10.1016/j.rineng.2023.101213.
[26] S. Ata, Comprehensive evaluation of a gas turbine-based multi-generation system for power, heating, cooling, freshwater, hydrogen and ammonia: 4E assessment and multi-objective optimization with RSM desirability approach, Renewable Energy, 246 (2025) 122900. https://doi.org/10.1016/j.renene.2025.122900.
[27] Y. Qiu, X. Lan, J. Liu, G. Wang, Z. Huang, Optimization design of nozzle parameters un

der the condition of submerged water jet breaking soil based on response surface method, Applied Ocean Research, 154 (2025) 104369. https://doi.org/10.1016/j.apor.2024.104369.
[28] X. Tang, Y. Yue, Y. Shen, Prediction of separation efficiency in gas cyclones based on RSM and GA-BP: Effect of geometry designs, Powder Technology, 416 (2023) 118185. https://doi.org/10.1016/j.powtec.2022.118185.
[29] G. Cao, G. Sun, S. Yuan, Y. Yue, Y. Wu, Multiobjective Optimization of Spiral Guide Vanes for Boosting Separation Performance of Cyclone Separators, Industrial & Engineering Chemistry Research, 63 (2024) 9162-9175. https://doi.org/10.1021/acs.iecr.4c00172.
[30] H. Li, L. Yang, D. Zhang, C. Tao, X. He, C. Xie, C. Li, Z. Du, T. Xiao, Z. Li, H. Wang, Design and optimization of a high-speed maize seed guiding device based on DEM-CFD coupling method, Computers and Electronics in Agriculture, 227 (2024) 109604. https://doi.org/10.1016/j.compag.2024.109604.
[31] Q. Al-Tashi, S.J. Abdulkadir, H.M. Rais, S. Mirjalili, H. Alhussian, Approaches to Multi-Objective Feature Selection: A Systematic Literature Review, Ieee Access, 8 (2020) 125076-125096. https://doi.org/10.1109/access.2020.3007291.
[32] V. Pandey, Komal, H. Dincer, A review on TOPSIS method and its extensions for different applications with recent development, Soft Computing, 27 (2023) 18011-18039. https://doi.org/10.1007/s00500-023-09011-0.
[33] R. Jiang, S. Ci, D. Liu, X. Cheng, Z. Pan, A Hybrid Multi-Objective Optimization Method Based on NSGA-II Algorithm and Entropy Weighted TOPSIS for Lightweight Design of Dump Truck Carriage, Machines, 9 (2021) 156. https://doi.org/10.3390/machines9080156.
[34] L. Sun, B. Chen, Q. Zhou, D. Zhao, Multi-objective optimization of wire cutting process parameters for Ti-6Al-4V alloy is performed using NSGA-II and EWM-TOPSIS optimized artificial neural network, Proceedings of the Institution of Mechanical Engineers Part C-Journal of Mechanical Engineering Science, 239 (2025) 3772-3789. https://doi.org/10.1177/09544062251315035.
[35] J. Lv, Y. Sun, J. Lin, X. Luo, P. Li, Multi-objective optimization research of printed circuit heat exchanger based on RSM and NSGA-II, Applied Thermal Engineering, 254 (2024) 123925. https://doi.org/10.1016/j.applthermaleng.2024.123925.
[36] X. Wei, Y. Qian, Y. Li, M. Yao, D. Qian, Z. Gong, Multi-objective optimization of the TPMS-Fin three-fluid heat exchanger for vehicles using RSM-NSGA-III, Energy, 328 (2025) 136462. https://doi.org/10.1016/j.energy.2025.136462.
[37] S. Cloete, S.T. Johansen, S. Amini, Performance evaluation of a complete Lagrangian KTGF approach for dilute granular flow modelling, Powder Technology, 226 (2012) 43-52. https://doi.org/10.1016/j.powtec.2012.04.010.
[38] D. Sun, Second-order moment of kinetic theory of granular flow for multi-type particles, Powder Technology, 444 (2024) 120029. https://doi.org/10.1016/j.powtec.2024.120029.
[39] X. Chen, J. Wang, A comparison of two-fluid model, dense discrete particle model and CFD-DEM method for modeling impinging gas-solid flows, Powder Technology, 254 (2014) 94-102. https://doi.org/10.1016/j.powtec.2013.12.056.